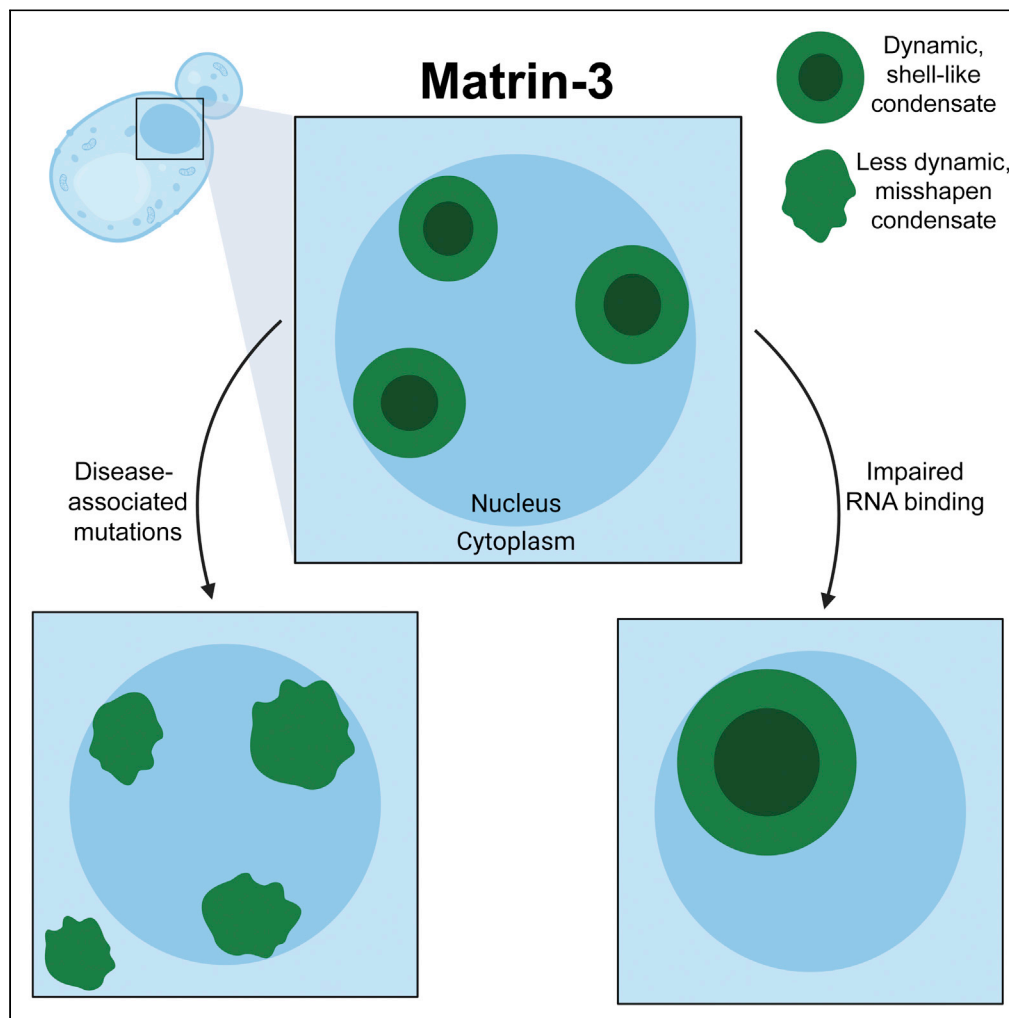


Article

Molecular determinants and modifiers of Matrin-3 toxicity, condensate dynamics, and droplet morphology



Macy L. Sprunger,
Ken Lee, Brian S.
Sohn, Meredith E.
Jackrel

mjackrel@wustl.edu

Highlights

Matrin-3 forms liquid, dynamic, shell-like nuclear condensates in yeast

Disease-associated mutations in Matrin-3 impair condensate dynamics and morphology

Proteotoxicity of Matrin-3 in yeast is driven by its RNA-recognition motifs

Potentiated Hsp104 variants can suppress the toxicity of Matrin-3^{WT} and mutants

Sprunger et al., iScience 25,
103900
March 18, 2022 © 2022 The
Author(s).
[https://doi.org/10.1016/
j.isci.2022.103900](https://doi.org/10.1016/j.isci.2022.103900)

Article

Molecular determinants and modifiers of Matrin-3 toxicity, condensate dynamics, and droplet morphology

Macy L. Sprunger,¹ Ken Lee,¹ Brian S. Sohn,¹ and Meredith E. Jackrel^{1,2,*}

SUMMARY

Matrin-3 (MATR3) is a DNA- and RNA-binding protein implicated in amyotrophic lateral sclerosis (ALS), frontotemporal dementia (FTD), and distal myopathy. Here, we report the development of a yeast model of MATR3 proteotoxicity and aggregation. MATR3 is toxic and forms dynamic shell-like nuclear condensates in yeast. Disease-associated mutations in MATR3 impair condensate dynamics and disrupt condensate morphology. MATR3 toxicity is largely driven by its RNA-recognition motifs (RRMs). Further, deletion of one or both RRM domains drives coalescence of these condensates. Aberrant phase separation of several different RBPs underpins ALS/FTD, and we have engineered Hsp104 variants to reverse this misfolding. Here, we demonstrate that these same variants also counter MATR3 toxicity. We suggest that these Hsp104 variants which rescue MATR3, TDP-43, and FUS toxicity might be employed against a range of ALS/FTD-associated proteins. We anticipate that our yeast model could be a useful platform to screen for modulators of MATR3 misfolding.

INTRODUCTION

Amyotrophic lateral sclerosis (ALS) is a progressive neurodegenerative disorder which results in the degeneration of upper and lower motor neurons, leading to atrophy of the skeletal muscles, and ultimately paralysis and death (Ling et al., 2013; Robberecht and Philips, 2013; Taylor et al., 2016). Frontotemporal dementia (FTD) is a related disorder which affects the frontal and temporal cortices, leading to personality, behavioral, and language changes (Ling et al., 2013). ALS and FTD lie within a disease spectrum, with clinical, pathological, and genetic overlap (Ling et al., 2013; Robberecht and Philips, 2013; Taylor et al., 2016). The implication of multiple RNA-binding proteins (RBPs) in ALS/FTD, including TDP-43 (Neumann et al., 2006), FUS (Kwiatkowski et al., 2009; Vance et al., 2009), hnRNPA1 (Kim et al., 2013), hnRNPA2B1 (Kim et al., 2013), EWSR1 (Couthouis et al., 2012; Neumann et al., 2011), TAF15 (Couthouis et al., 2011; Neumann et al., 2011), ATXN2 (Elden et al., 2010), and MATR3 (Johnson et al., 2014), suggests that RNA dysregulation is a key mechanism underpinning ALS/FTD pathogenesis (King et al., 2012). These RBPs are also characterized by the presence of large intrinsically disordered regions (IDRs) which can drive liquid-liquid phase separation (LLPS) (Franzmann and Alberti, 2019; Sprunger and Jackrel, 2021). Because of their disordered nature and their accumulation at high concentrations upon LLPS, these RBPs are prone to misfold and aggregate, and accumulations of misfolded RBPs are the pathological hallmark of ALS/FTD (Ling et al., 2013; Taylor et al., 2016).

Matrin-3 (MATR3) is a DNA- and RNA-binding nuclear matrix protein which is highly conserved (Belgrader et al., 1991). MATR3 functions in the DNA damage response, transcription, splicing, RNA degradation, mRNA export, and maintenance of the nuclear framework through interactions with nuclear laminas (Boehringer et al., 2017; Coelho et al., 2015; Depreux et al., 2015; Hibino et al., 2000; Leonard et al., 2003; Salton et al., 2010, 2011; Zeitz et al., 2009). A missense mutation, MATR3^{S85C}, leads to autosomal dominant distal myopathy with vocal cord and pharyngeal weakness (VCPDM), many cases of which have subsequently been reclassified as ALS (Feit et al., 1998; Johnson et al., 2014; Senderek et al., 2009). Exome sequencing has identified 13 additional MATR3 mutations in familial ALS and ALS/FTD cases (Johnson et al., 2014; Leblond et al., 2016; Lin et al., 2015; Marangi et al., 2017; Narain et al., 2019; Origone et al., 2015). Wild-type MATR3 displays physiological granular nuclear staining in neurons with more intense nuclear staining and some diffuse cytoplasmic redistribution in ALS patient neurons (Johnson et al., 2014). In ALS patients with mutations in FUS, and in those harboring the C9orf72 hexanucleotide repeat expansion, pathological inclusions of wild-type MATR3 have been noted (Johnson et al., 2014; Tada et al., 2018). Further, MATR3

¹Department of Chemistry, Washington University, St. Louis, MO 63130, USA

²Lead contact

*Correspondence: mjackrel@wustl.edu

<https://doi.org/10.1016/j.isci.2022.103900>



has been found to colocalize with TDP-43 inclusions in a significant subset of patient samples (Tada et al., 2018). Although MATR3 mutations have a low frequency, the pathology of both mutant and wild-type MATR3 in diverse forms of ALS/FTD suggests that MATR3 could play a key role in pathogenesis.

The role of MATR3 and its pathogenic mutations have recently been investigated in several model systems (Gallego-Iradi et al., 2015; Kao et al., 2020; Malik et al., 2018; Mensch et al., 2018; Moloney et al., 2018; Ramesh et al., 2020; van Bruggen et al., 2021; Zhang et al., 2019). Homozygous knockout of MATR3 in mice is embryonic lethal, suggesting that MATR3 is essential for development (Quintero-Rivera et al., 2015). Overexpression of MATR3^{WT}, MATR3^{S85C}, or MATR3^{F115C} as well as knock-in of MATR3^{S85C} in mice results in motor and neuronal defects (Kao et al., 2020; Moloney et al., 2018; Zhang et al., 2019). However, knock-in of MATR3^{F115C} did not lead to muscle or neuronal pathology in mice, suggesting that MATR3^{F115C} may not be a causative mutation in ALS/FTD (van Bruggen et al., 2021). Expression of MATR3^{WT} in primary neurons and *Drosophila* is associated with increased risk of death or shortened lifespan, and disease-associated mutations to MATR3 subtly enhance this effect (Malik et al., 2018; Ramesh et al., 2020; Zhao et al., 2020). In myoblasts and neurons, MATR3 mutants did not show altered nucleocytoplasmic localization or protein expression levels (Gallego-Iradi et al., 2015; Malik et al., 2018; Mensch et al., 2018). RNA-binding deficient MATR3 can undergo LLPS with localization to large nuclear puncta, and introduction of S85C to RNA-binding deficient MATR3 constructs decreases condensate dynamics (Gallego-Iradi et al., 2019; Iradi et al., 2018; Malik et al., 2018; Mensch et al., 2018). While much has been learned about MATR3, there have been some conflicting findings and many key questions remain unresolved. For instance, in primary neurons, it was shown that MATR3 zinc fingers drive toxicity, while conflicting results in a *Drosophila* model suggest that MATR3 RRM domains drive toxicity (Malik et al., 2018; Ramesh et al., 2020).

While recent studies have revealed important insights into MATR3 function, key gaps remain regarding the link between MATR3 and ALS/FTD pathology. A simple, genetically tractable model with exogenous MATR3 expression would be useful for investigating the contribution of MATR3 domains and mutations to MATR3 toxicity, aggregation, and liquid-liquid phase separation. Here, we have developed a budding yeast, *Saccharomyces cerevisiae*, model system to investigate the molecular determinants of MATR3 proteotoxicity. Numerous pathways relevant to human disease are highly conserved in *S. cerevisiae*, and yeast models have proven useful in studying diverse human disorders including ALS/FTD (Elden et al., 2010; Johnson et al., 2008; Ju et al., 2011; Khurana and Lindquist, 2010; Ryan et al., 2019; Sun et al., 2011; Treusch et al., 2011). We find that overexpression of MATR3 in yeast recapitulates key features of MATR3 expression in other systems, including nuclear localization and toxicity. Using this system we find that MATR3 forms dynamic shell-like nuclear condensates, and that the formation of these structures is impaired upon introduction of ALS/FTD-associated mutations in MATR3. By studying a series of MATR3 constructs, we delineate key sequence-specific elements driving MATR3 toxicity, localization, aggregation, and phase separation. Furthermore, we demonstrate that engineered Hsp104 variants that can suppress the toxicity and mislocalization of TDP-43 and FUS (Jackrel et al., 2014; Jackrel and Shorter, 2014a; Yokom et al., 2016) can also suppress the toxicity induced by MATR3 and its mutants, thereby simultaneously countering the misfolding of three different proteins which may misfold together in ALS/FTD patients. Our results suggest that MATR3 toxicity arises from aberrant protein misfolding and consequent proteotoxic stress. We therefore propose that this yeast model of MATR3 can be utilized as a platform for studying the underpinnings of MATR3 toxicity, and for screening for modulators of MATR3 phase separation and toxicity. Further, we suggest that engineered Hsp104 variants could be employed to simultaneously combat a range of proteins that misfold in ALS/FTD, including MATR3.

RESULTS

Matrin-3 is an intrinsically disordered RNA-binding protein that is toxic when overexpressed in yeast

MATR3 is a nuclear matrix protein that is 847 amino acids long. MATR3 contains two zinc finger (ZF) motifs, two RNA-recognition motifs (RRMs), and a nuclear localization signal (NLS) (Malik et al., 2018) (Figure 1A). The FoldIndex algorithm (Prilusky et al., 2005), which analyzes hydrophobicity and net charge per residue, predicts that most regions outside of these annotated domains are unfolded (Figure 1B). Fourteen different pathogenic mutations have been identified in MATR3, including S85C, F115C, P154S, and T622A, each of which are implicated in familial ALS/FTD, although it remains controversial if the F115C mutation drives ALS/FTD (Johnson et al., 2014; Leblond et al., 2016; Lin et al., 2015; Marangi et al., 2017; Origone et al., 2015; Senderek et al., 2009; van Bruggen et al., 2021; Xu et al., 2016). Most of these pathogenic

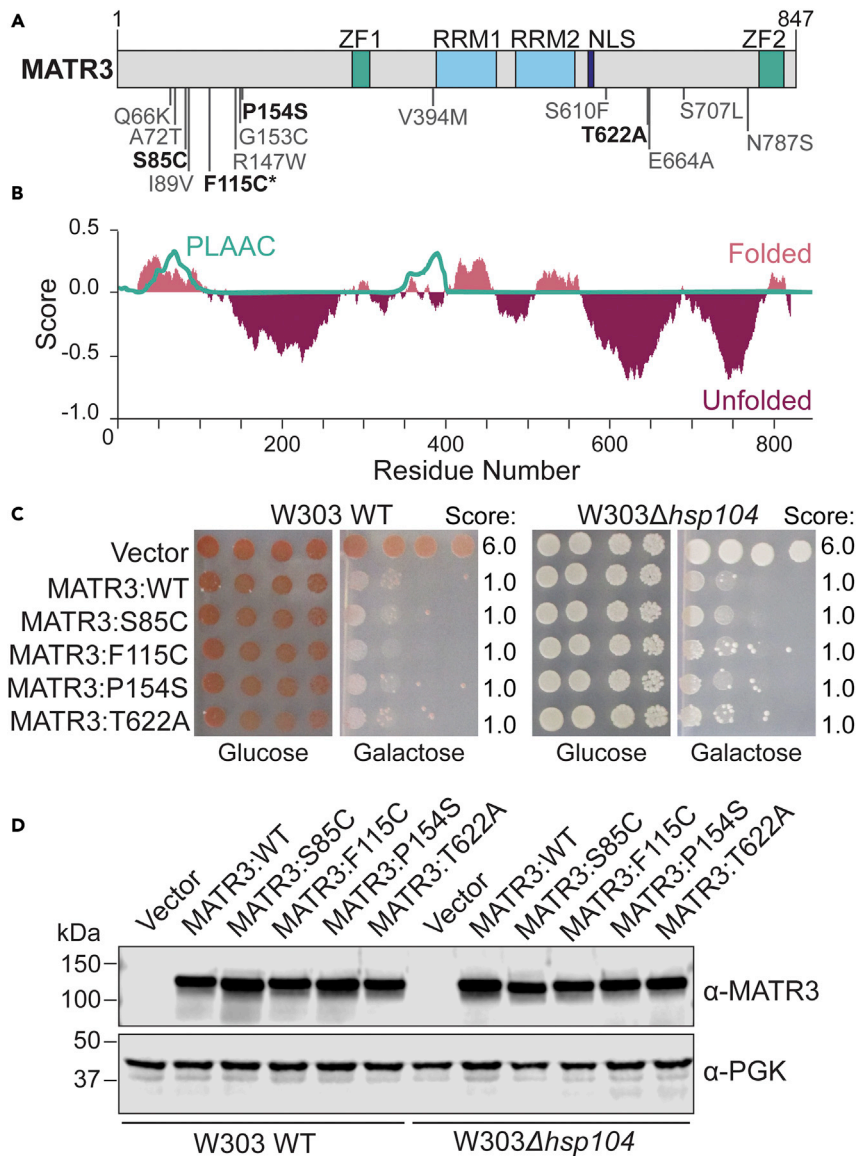


Figure 1. MATR3 is an intrinsically disordered protein that is toxic in yeast but does not display prion-like properties

(A) Domain map of MATR3. The zinc finger (ZF) domains, RNA-recognition motifs (RRMs), and nuclear localization signal (NLS) are highlighted. Mutations of interest in MATR3 are shown, with mutations used in this study displayed in bold. Asterisk indicates a patient-associated mutation which may not be causative of disease.

(B) Computational analysis of MATR3 sequence using the FoldIndex algorithm (pink and dark pink), and PLAAC algorithm (teal) (Lancaster et al., 2014; Prilusky et al., 2005). The output score of each program is plotted against the MATR3 sequence. FoldIndex uses net charge per residue and hydrophobicity to predict whether a region is folded (positive, pink) or unfolded (negative, dark pink). This analysis predicts the presence of large disordered regions throughout the MATR3 sequence. PLAAC analyzes amino acid composition to identify regions of similar composition to known yeast prion proteins, with prion-like domains indicated by a score of one (Lancaster et al., 2014). By this analysis, MATR3 is not predicted to have a prion-like domain.

(C) W303WT and W303Δhsp104 yeast were transformed with the indicated pAG413GAL-MATR3 variant or vector control. Strains were serially diluted 5-fold and spotted in duplicate onto glucose (non-inducing) and galactose (inducing) media. Scores are based on number of spots from an average of at least three biological replicates.

(D) Strains from C were induced for 5 h, lysed, and immunoblotted for MATR3 and 3-phosphoglycerate kinase (PGK; loading control). See also Figure S1.

mutations are found in the largely disordered regions of the protein, and clustered near the N-terminus and C-terminus (Figure 1A). Similarly in other ALS-associated RBPs including TDP-43, FUS, hnRNPA1, and hnRNPA2B1, pathogenic mutations are clustered in the disordered prion-like domains (PrLDs) (King et al., 2012; Taylor et al., 2016). Therefore, we next investigated if MATR3 contains prion-like character. Using the Prion-Like Amino Acid Composition algorithm (PLAAC) (Lancaster et al., 2014) we found that, unlike TDP-43 and FUS, MATR3 lacks a predicted PrLD (Figures 1B and S1).

TDP-43 and FUS are nuclear RNA-binding proteins with PrLDs that mislocalize to cytoplasmic inclusions in degenerating motor neurons of ALS patients (Robberecht and Philips, 2013; Taylor et al., 2016). Understanding of the molecular requirements driving aberrant LLPS and aggregation of these and other proteins, as well as modifiers of these properties, has been empowered by use of yeast model systems (Becker et al., 2017; Elden et al., 2010; Johnson et al., 2008, 2009; Ju et al., 2011; Outeiro and Lindquist, 2003; Sun et al., 2011). Therefore, we sought to investigate the toxicity and localization of MATR3 in yeast, which lack a MATR3 homolog. We inserted the human MATR3 sequence and a subset of ALS/FTD-linked MATR3 mutants into the centromeric pAG413GAL-ccdB vector (Alberti et al., 2007) under control of the tightly regulated galactose-inducible promoter, allowing for inducible expression and passaging without toxicity. We noted that MATR3^{WT} was highly toxic when expressed in yeast, as were MATR3^{S85C}, MATR3^{F115C}, MATR3^{P154S}, and MATR3^{T622A} (Figure 1C). Thus, our yeast model recapitulates the highly toxic expression of wild-type MATR3 that has been observed in primary neurons and *Drosophila* models (Malik et al., 2018; Ramesh et al., 2020; Zhao et al., 2020). We do not observe a subtle increase in toxicity upon expression of the MATR3 mutants similar to that observed in primary neurons (Malik et al., 2018), which is likely due to the already very high toxicity of the wild-type protein in yeast. We also plated these strains on a mixture of sucrose with galactose to decrease MATR3 expression levels, and consequently toxicity, but still did not observe enhanced toxicity of the MATR3 mutants. Overall, the similarities we observe upon expression of MATR3 between yeast and primary neurons suggest that yeast can be used as a simple, yet relevant, model to study MATR3 misfolding.

We next aimed to better understand if MATR3 functions as a prion in yeast. Endogenous yeast prions are regulated by the native AAA+ ATPase Hsp104, which is required for yeast prion propagation and toxicity (Krobitsch and Lindquist, 2000; Parsell et al., 1994; Patino et al., 1996; Satpute-Krishnan et al., 2007). It has been shown that expression of a fragment of the huntingtin protein harboring a polyglutamine expansion is toxic in yeast, but that this toxicity is dependent upon the presence of the yeast prion [RNQ⁺] and the prion disaggregase Hsp104 (Duennwald et al., 2006; Krobitsch and Lindquist, 2000). We therefore tested the dependence of MATR3 toxicity on Hsp104 by comparing toxicity of MATR3 in W303^{WT} and W303 Δ *hsp104* yeast strains (Figure 1C). MATR3 toxicity was similar in both strains, indicating that the presence of Hsp104 and its prion propagation activity does not modulate MATR3 toxicity. Despite the presence of a PrLD, TDP-43 and FUS toxicity in yeast is also independent of Hsp104 (Jackrel et al., 2014; Johnson et al., 2008). Although TDP-43 and FUS are not known to function as yeast prions, these PrLDs are thought to be crucial in regulating their role in LLPS (Franzmann and Alberti, 2019; Sprunger and Jackrel, 2021). Using immunoblotting, we confirmed consistent MATR3 protein expression in each of the strains (Figure 1D). Thus, we conclude that our yeast system can be used as a relevant model to study MATR3 toxicity in a highly tractable manner.

MATR3 forms nuclear puncta in yeast

To further study the properties of MATR3 in yeast, we used fluorescence microscopy. Here, we employed the pAG423GAL-ccdB-GFP plasmid to drive higher levels of MATR3 expression and to append a C-terminal GFP tag for visualization. We first confirmed that toxicity was similar to that of the untagged constructs (Figures 1 and 2A), and that expression levels were similar across the strains (Figure 2B). We observed that MATR3^{WT}-GFP formed multiple round puncta in the nuclei (Figure 2C), which appear similar to the nuclear staining reported upon MATR3 expression in *Drosophila*, primary neurons, and mammalian cells (Gallego-Irardi et al., 2015, 2019; Malik et al., 2018; Ramesh et al., 2020). For MATR3^{S85C}, we again observed accumulation of multiple foci, but these appeared less round than the MATR3^{WT} puncta, and were not fully restricted to the nucleus. Similar irregularities were observed in the shape of MATR3^{P154S} and MATR3^{T622A} foci, while MATR3^{F115C} puncta were more round, similar to those of MATR3^{WT}. To analyze these puncta more closely, we imaged these cells using confocal microscopy. We again observed that MATR3 formed round puncta, while MATR3^{S85C}, MATR3^{P154S}, and MATR3^{T622A} puncta appeared misshapen (Figure 2D). We quantified the differences in foci shapes by calculating the circularity ratio of each focus (Figure 2E). We found that MATR3^{S85C}, MATR3^{P154S}, and MATR3^{T622A} all had significantly lower circularity ratios than

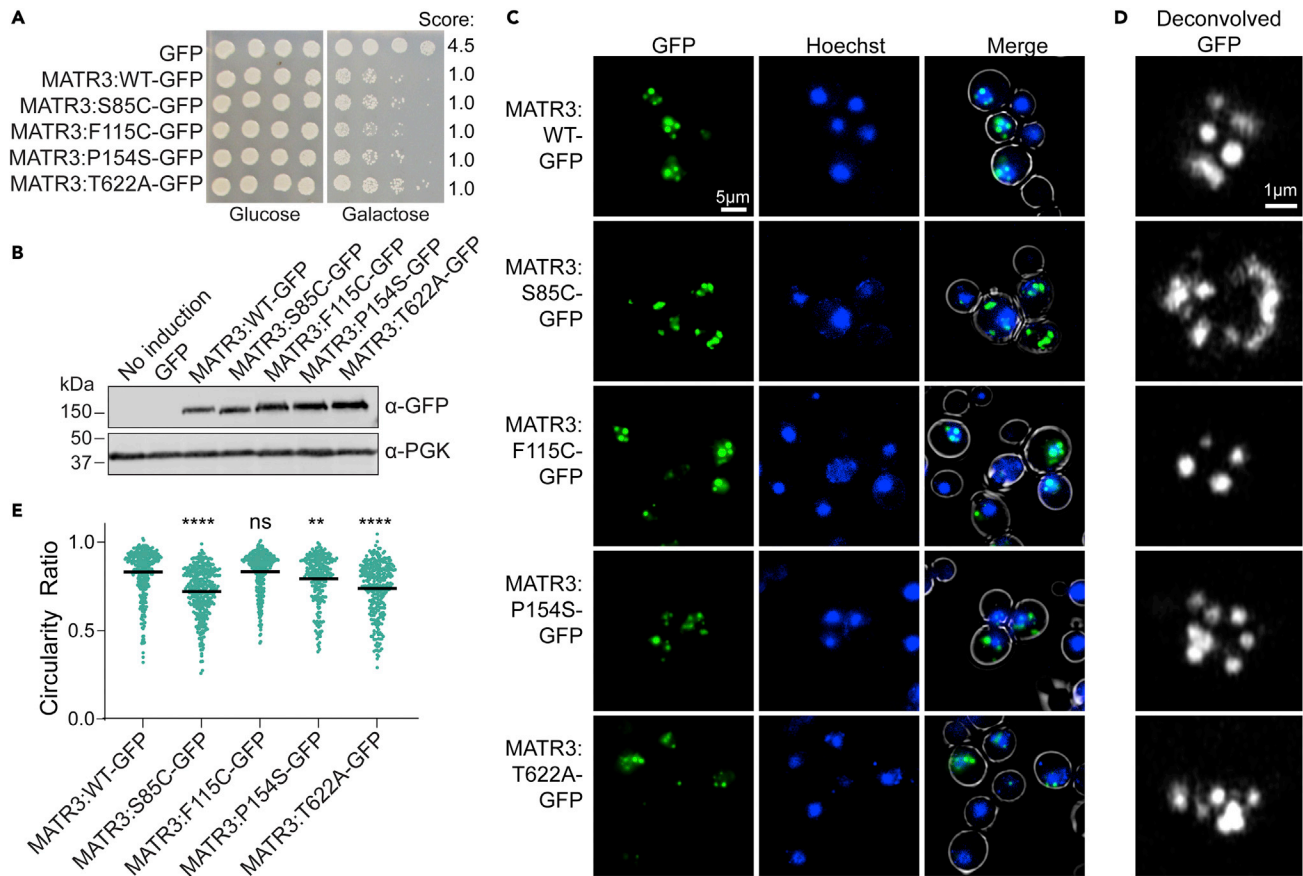


Figure 2. MATR3 forms round nuclear puncta in yeast, while some MATR3 mutants form misshapen puncta

(A) W303Δ*hsp104* yeast were transformed with the indicated pAG423GAL-MATR3-GFP variant or vector control. Strains were serially diluted 5-fold and spotted in duplicate on glucose (non-inducing) and galactose (inducing) media. Scores are based on number of spots from an average of at least three biological replicates.

(B) Strains from A were induced for 5 h, lysed, and immunoblotted for GFP (mouse) and PGK (loading control).

(C) Strains from A were induced for 5 h, stained with Hoechst dye, and imaged. Representative images are shown. Merge channel includes GFP, Hoechst, and bright field images. Scale bar, 5 μm.

(D) Strains from A were imaged at higher resolution using a confocal microscope with Airyscan deconvolution (Airyscan parameter 2.7). Representative images are shown. Scale bar, 1 μm.

(E) Circularity ratio of foci of MATR3-GFP (N = 233 cells), MATR3:S85C-GFP (N = 241 cells), MATR3:F115C-GFP (N = 252 cells), MATR3:P154S-GFP (N = 167 cells), MATR3:T622A-GFP (N = 245 cells) from experiments in D. Results were compared to those for the MATR3-GFP strain using a one-way ANOVA with a Dunnett's multiple comparisons test (individual data points are shown as dots, bars show means, **p < 0.005, ****p < 0.0001).

MATR3^{WT}, indicating that their puncta are less round. This affect was most notable for MATR3^{S85C}, and least severe for MATR3^{P154S}. MATR3^{F115C} puncta showed no significant difference in circularity ratio as compared to MATR3^{WT}, supporting recent studies suggesting that this mutation does not significantly perturb MATR3 and, therefore, it may not be a causative mutation in ALS/FTD (van Bruggen et al., 2021). The rounded appearance of the MATR3^{WT} puncta suggests that these structures may be dynamic liquid-like condensates. The misshapen puncta of MATR3^{S85C}, MATR3^{P154S}, and MATR3^{T622A} that we observe may be due to perturbed phase separation, perhaps reflecting decreased dynamics within the puncta and conversion to a gel- or solid-like state.

MATR3 mutations impair condensate dynamics

To investigate the effect of MATR3 mutations on condensate properties, we performed fluorescence recovery after photobleaching (FRAP) experiments with a superresolution microscope (Figure 3A). When studying the round puncta of MATR3^{WT} and MATR3^{F115C} at this higher resolution, we observe that these spherical droplets appear devoid of MATR3 in the center (Figure 3A, pre-bleach images). These structures are reminiscent of the

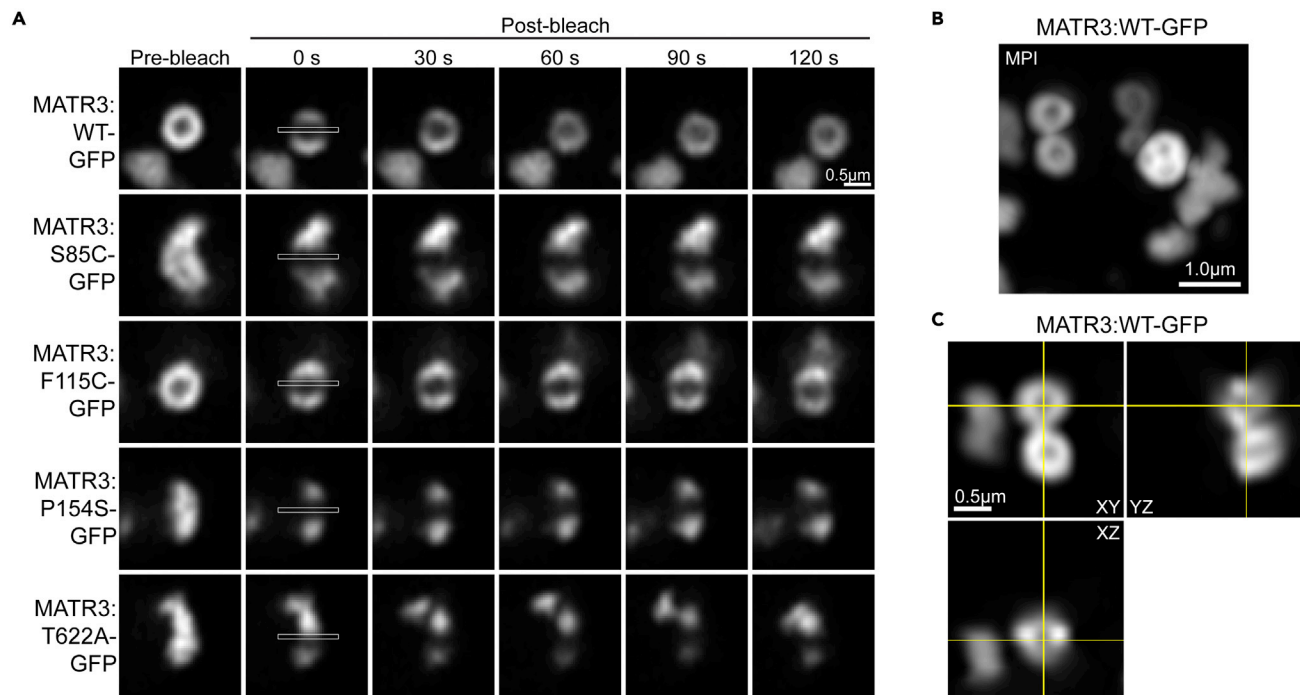


Figure 3. MATR3^{WT} forms dynamic liquid-like shell structures while MATR3 mutations impair droplet dynamics

(A) FRAP of MATR3-GFP and mutants. W303Δ*hsp104* yeast were transformed with the indicated pAG423GAL-MATR3-GFP variants, induced for 5 h, immobilized on an agarose pad, and imaged on a superresolution Zeiss LSM 880 Airyscan Fast confocal microscope with deconvolution (Airyscan parameter 6.9). MATR3-GFP foci were photobleached in a 1 × 25 pixel line, and recovery was monitored over 2 min. MATR3^{WT} displays full recovery within 2 min. MATR3^{F115C} showed partial recovery by 2 min while MATR3^{S85C}, MATR3^{P154S}, and MATR3^{T622A} do not recover. Images from one trial are shown, which are representative of at least ten trials per strain. White box indicates bleached region. Scale bar, 0.5 μm.

(B) MATR3^{WT}-GFP yeast were induced for 5 h and imaged by superresolution confocal microscopy with deconvolution (Airyscan parameter 7.9). The maximum peak intensity of a z stack is displayed. Scale bar, 1 μm.

(C) Expanded orthogonal view of a focus from the same field of view depicted in (B) Scale bar, 0.5 μm. See also [Video S1](#).

LLPS intranuclear anisosomes, or shell-like spherical condensates, that form from RNA binding-deficient TDP-43 (Yu et al., 2021), which can also appear as “bubbles” (Schmidt and Rohatgi, 2016) or nuclear bodies (Wang et al., 2020). Further examination of MATR3^{WT}-GFP cells confirmed that most of the puncta we observe are these spherical shell-like structures, which are also devoid of MATR3 in the center (Figures 3B and 3C). Likely these structures form because MATR3, and presumably some of its binding partners, are normally absent from yeast and so expression of MATR3 in yeast mimics an RNA-binding deficient state. In contrast to MATR3^{WT} puncta, MATR3^{S85C}, MATR3^{P154S}, and MATR3^{T622A} puncta appear to be misshapen and do not have a shell-like structure devoid of MATR3 in the center (Figure 3A, pre-bleach images). On monitoring the recovery of these structures after photobleaching, we observe rapid recovery of the MATR3^{WT} structures, which fully recover by 60 s (Figure 3A). Similarly, we observe partial recovery of MATR3^{F115C} shells within 2 min following photobleaching. However, no recovery was observed after photobleaching MATR3^{S85C}, MATR3^{P154S}, or MATR3^{T622A} (Figure 3A and [Video S1](#)). We were unable to quantify recovery due to movement of the structures within the immobilized cells ([Video S1](#)). These results confirm our findings from the circularity measurements, and support our hypothesis that MATR3^{WT} puncta are dynamic liquid-like droplets. MATR3^{F115C} puncta are also liquid-like condensates but with slightly impaired dynamics as compared to MATR3^{WT}. The more notably impaired dynamics characteristic of MATR3^{S85C}, MATR3^{P154S}, and MATR3^{T622A} indicate that these proteins have undergone an aberrant phase transition to a gel- or solid-like structure. Importantly our studies are, to our knowledge, the first to show that disease-associated mutations in MATR3 can impair condensate dynamics in the full-length protein.

MATR3 displays decreased solubility in yeast

MATR3^{S85C} has been shown to form insoluble, detergent-resistant accumulations in lymphoblasts, HEK293T cells, primary neurons, and *Drosophila* while MATR3^{WT} is similarly insoluble under thermal or

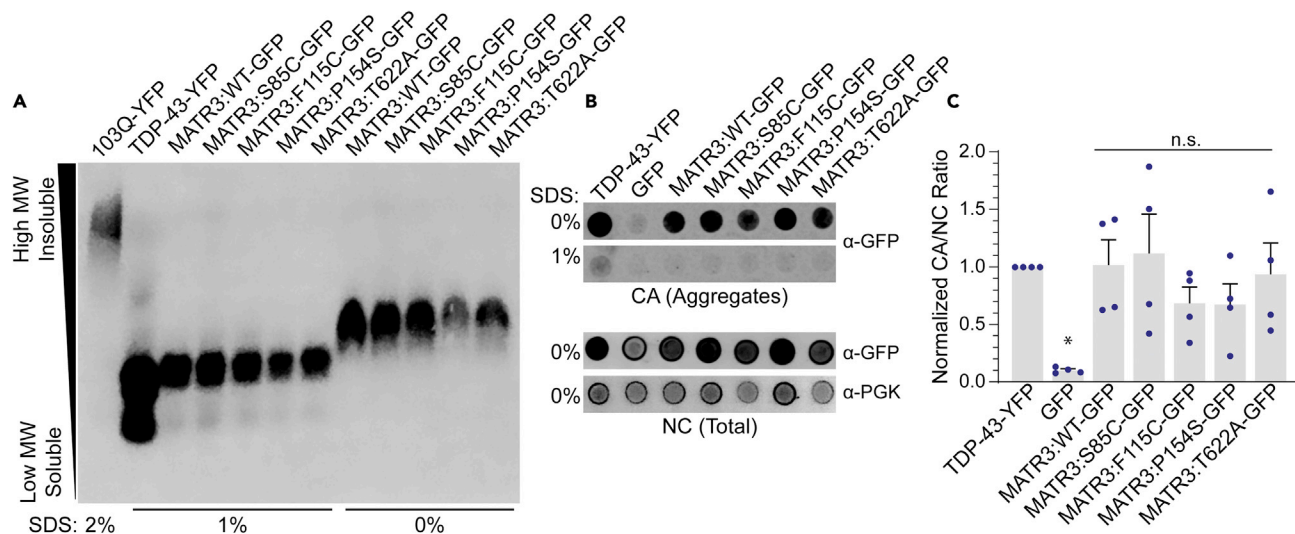


Figure 4. MATR3 and MATR3 variants form insoluble species that are subtly resistant to detergent

(A) W303 Δ hsp104 yeast were transformed with pAG423GAL-MATR3-GFP or the indicated MATR3 mutants. W303WT pAG303GAL-103Q-YFP, W303 Δ hsp104 pAG303GAL-TDP-43-YFP were used as controls. Strains were induced for 5 h, lysed under native conditions, and analyzed by semi-denaturing detergent agarose gel electrophoresis (SDD-AGE) with the indicated SDS concentrations. MATR3 was detected via immunoblotting against GFP (mouse).

(B) Filter retention assays were performed on the same yeast lysates used in (A). Lysates were applied to cellulose acetate (CA) and nitrocellulose (NC) membranes in parallel and immunoblotted for GFP (rabbit) or PGK.

(C) Quantification of immunoblots from B using 0% SDS samples. The ratio of GFP detection on the CA vs. NC membrane was calculated and normalized to TDP-43-YFP levels. Results were compared to those for the TDP-43-YFP strain using a one-way ANOVA with a Dunnett's multiple comparisons test (individual data points are shown as dots, bars show means \pm SEM, N = 4, *p < 0.05).

proteotoxic stress conditions (Hayes et al., 2020; Johnson et al., 2014; Malik et al., 2018; Ramesh et al., 2020; Senderek et al., 2009; Xu et al., 2012). We therefore assessed the solubility of MATR3^{WT} and MATR3 mutants in yeast. Here, we performed semi-denaturing detergent-agarose gel electrophoresis (SDD-AGE), which is a technique that resolves amyloid and other higher molecular weight (MW) insoluble aggregates from soluble proteins based on size and solubility (Halfmann and Lindquist, 2008). We performed SDD-AGE on yeast lysates under native conditions from strains expressing MATR3^{WT} and its variants, including TDP-43-YFP and a polyglutamine expansion (103Q-YFP) as controls (Figure 4A). As has been shown previously, the polyglutamine lysate shows a characteristic smear in the upper portion of the gel, indicative of higher MW, insoluble species (Halfmann and Lindquist, 2008). TDP-43 displays a faint smear in a region of soluble, lower MW species than polyglutamine. MATR3 and each of the variants all displayed soluble, low MW smears similar to that of TDP-43. We also performed this assay with no added SDS and still observed accumulation of MATR3 low MW species. Both with and without SDS, MATR3^{WT} and its variants display similar migration patterns, indicating that the pathogenic mutations may not fully destabilize MATR3.

To corroborate our results from the SDD-AGE assays, we also performed filter retention assays (Alberti et al., 2010). Here, cells are lysed with glass beads under native conditions. Extracts are then passed over a non-binding cellulose acetate (CA) membrane. Soluble proteins pass through this membrane while insoluble materials will bind the membrane. To account for total protein, extracts are passed in parallel over a nitrocellulose (NC) membrane. The membranes can then be probed by immunoblotting, and the ratio of protein bound to the CA to NC membranes is calculated. We again performed these assays with both 0 and 1% SDS (Figure 4B). In the absence of SDS, we find that TDP-43 forms insoluble accumulations that bind the CA membrane, while for a strain expressing GFP alone, little binding to the CA membrane is detected. Similar to the strain expressing TDP-43, we observe that MATR3^{WT} and its mutants bind heavily to the CA membrane. In the presence of 1% SDS, we observe very little binding to the CA membrane for any of the strains. We quantified these effects by calculating the ratio of protein bound to the CA versus NC membrane (Figure 4C). Compared to TDP-43-YFP, untagged GFP was significantly more soluble while MATR3^{WT} and its mutants were similarly soluble to TDP-43-YFP. We conclude that the solubility of MATR3^{WT} and MATR3 variants is similar to that of TDP-43, and that pathogenic mutations to MATR3 do not significantly alter MATR3 solubility. While we do not observe differences in MATR3 solubility in the cells

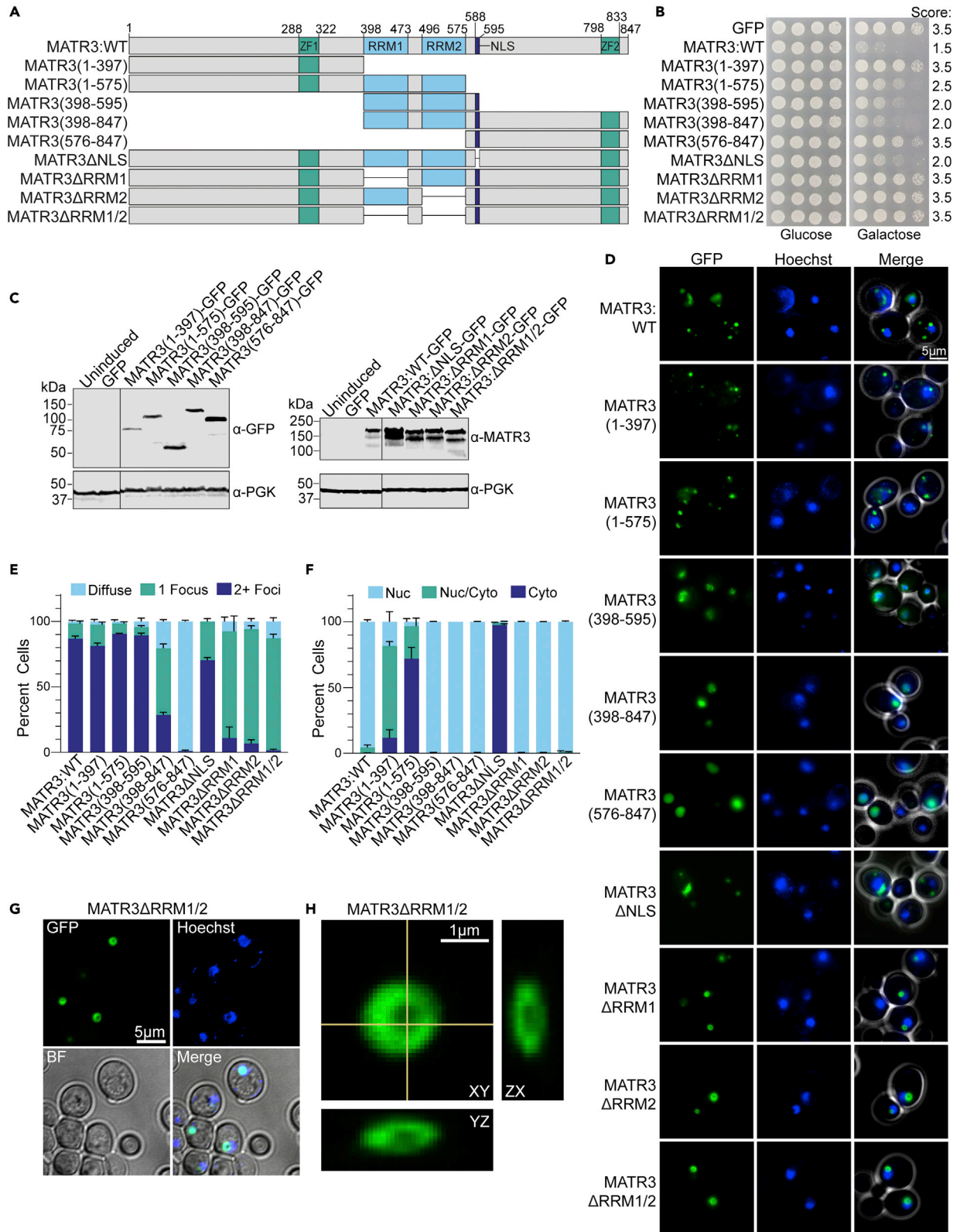


Figure 5. Molecular determinants of MATR3 toxicity, aggregation, and localization

(A) MATR3 domain map showing the constructs used in this study.

(B) W303 Δ hsp104 yeast was transformed with the indicated pAG423GAL-MATR3-GFP constructs or vector control. Strains were serially diluted 5-fold and spotted in duplicate on glucose (non-inducing) and galactose (inducing) media. Scores are based on number of spots from an average of at least three replicates.

(C) Strains from B were induced for 5h, lysed, and immunoblotted for MATR3, GFP (mouse), and PGK (loading control). Immunoblots were cropped to remove additional lanes for presentation purposes, and crop lines are marked with a line.

(D) Strains from B were induced for 5 h, stained with Hoechst dye, and imaged. Representative images are shown. Merge channel includes GFP, Hoechst, and bright field images. Scale bar, 5 μ m.

(E and F) Quantification of microscopy experiments shown in D. The percentages of cells with diffuse (light blue), one focus (teal), or multiple foci (dark blue) are quantified (E). The percentages of cells with nuclear (Nuc, light blue), nuclear and cytoplasmic (Nuc/Cyto, teal), or cytoplasmic (Cyto, dark blue) localization of MATR3-GFP is quantified (F). $N \geq 3$, with approximately 100 cells quantified per trial. Error bars show mean \pm SEM.

(G) pAG423GAL-MATR3 ^{Δ RRM1/2}-GFP yeast were induced for 5 h, stained with Hoechst dye, and imaged by confocal microscopy. A representative z slice is shown. Scale bar, 5 μ m.

(H) Expanded orthogonal view of a focus from the same strain depicted in (G) Scale bar, 1 μ m. See also [Figure S2](#).

harboring the dynamic shell-like condensates as compared to those with the solid-like condensates, these changes in LLPS may result in too subtle of a perturbation of solubility to be observed by SDD-AGE and filter retention assays, highlighting the importance of using a range of approaches to study biomolecular condensates.

Defining the regions of MATR3 that drive its toxicity and aggregation

We next leveraged the genetic tractability of yeast to probe the drivers of MATR3 toxicity and aggregation. We designed a series of MATR3 truncation constructs as GFP-fusions and tested their toxicity and aggregation ([Figure 5](#)). Here, we systematically removed the C-terminal region (MATR3(1–397) and MATR3(1–575)), the N-terminal region (MATR3(398–847) and MATR3(576–847)), part of both the N- and C-terminal regions (MATR3(398–595)), or the nuclear localization signal (NLS) (MATR3 Δ NLS) ([Figure 5A](#)). In assessing the toxicity of these constructs, we found that full-length MATR3 was the most toxic. MATR3(398–595), MATR3(398–847), and MATR3 Δ NLS were slightly less toxic, while MATR3(1–575) displayed only subtle toxicity ([Figure 5B](#)). MATR3(1–397) and MATR3(576–847) were both nontoxic, indicating that the RRM s are required for toxicity. MATR3(398–595), which contains only the RRM s and NLS, is nearly as toxic as the full-length construct, while MATR3(1–575) lacks the NLS and is only subtly toxic, suggesting that both RNA binding and nuclear localization are required for MATR3 toxicity. Further, the N- and C-terminal regions of MATR3 do not contribute to toxicity. These results also help to explain why the pathogenic mutations which fall outside of the RRM s and NLS do not modulate MATR3 toxicity.

We next confirmed expression of each MATR3 truncation construct by immunoblotting ([Figure 5C](#)). MATR3 typically runs approximately 30–40 kD higher than its calculated MW on SDS-PAGE, which we hypothesize is due to the highly acidic nature of its C-terminal region or post-translational modifications. We find that MATR3^{WT} (123.7 kD calculated, 160 kD observed), MATR3(398–847) (77.7 kD calculated, 120 kD observed), and MATR3(576–847) (57.1 kD calculated, 90kD observed) each run approximately 40 kD higher than their calculated MW. However, MATR3(1–397) (70.8 kD calculated, 75 kD observed), MATR3(1–575) (91.4 kD calculated, 100 kD observed) and MATR3(398–595) (52 kD calculated, 50kD observed), all of which lack the acidic C-terminal region, did not have similarly large discrepancies between their calculated and observed MW. These results support our hypothesis that the highly charged C-terminal region of MATR3 causes a shift in its apparent molecular weight.

Next, we studied the localization and foci formation of strains expressing these constructs ([Figures 5D–5F](#)). Full-length MATR3 displayed multiple round nuclear foci as we previously observed ([Figures 2C, 2D and 5D](#)). MATR3(1–397), MATR3(1–575), and MATR3 Δ NLS also drove accumulation of multiple foci per cell like the full-length construct, but unlike in the full-length construct, these foci were not restricted to the nucleus. This shift in localization is expected because all three of these constructs lack the NLS. However, MATR3(398–595), MATR3(398–847), and MATR3(576–847), which all contain the NLS identified by Malik et al., were all localized to the nucleus ([Malik et al., 2018](#)). Expression of the C-terminal constructs (MATR3(398–847) and MATR3(576–847)) both appeared to yield fewer foci per cell, with MATR3(576–847) accumulating almost exclusively in a diffuse nuclear pattern. Further, the patterns for MATR3(398–595) and MATR3(398–847) were highly similar, suggesting that the C-terminal region has little effect on foci formation. To confirm that these states represent distinct features, and that these puncta do not fuse or convert to a single larger structure, similar to the large puncta observed for MATR3(576–847), we imaged

a subset of strains over a time course (Figure S2), but observed no such changes. Overall, these experiments demonstrate that the intrinsically disordered N-terminal region plays the biggest role in the formation of foci, driving accumulation of multiple foci per cell, while the RRM2 also contribute to foci formation. However, MATR3(398–595), which lacks both the N- and C-terminal disordered regions, forms nuclear puncta. Our findings suggest that neither of these disordered regions is strictly required for foci formation. Further, MATR3 can be toxic when found in the nucleus or in the cytoplasm, although toxicity is greatest when MATR3 is restricted to the nucleus. In addition, aggregation alone is insufficient to drive toxicity.

To more carefully investigate the role of the two RRMs, we also tested constructs with 1, 2, or both RRMs deleted (Figure 5, constructs MATR3^{ΔRRM1}, MATR3^{ΔRRM2}, and MATR3^{ΔRRM1/2}). We found that none of these constructs were toxic in yeast, confirming that the RRMs are largely responsible for MATR3 toxicity (Figure 5B). Importantly, while prior studies have suggested that RRM2 primarily drives toxicity (Gallego-Iradi et al., 2019; Malik et al., 2018; Ramesh et al., 2020), we find that ablation of either RRM entirely ablates toxicity. We confirmed expression of each deletion construct (Figure 5C). Surprisingly, expression of each of these RRM deletion constructs showed nearly all cells harbor a single nuclear focus with a spherical shell-like structure similar to those formed by MATR3^{WT} and MATR3^{F115C} (Figures 5D–5F). To investigate this further, we examined these cells using confocal microscopy and found that MATR3 lacking either or both RRMs coalesced into one large shell-like spherical structure per nucleus, as compared to the multiple smaller shell-like structures observed for MATR3^{WT} and MATR3^{F115C} (Figures 5G and 5H). We therefore conclude that both RRMs are required for toxicity and that ablation of either RRM eliminates the formation of multiple nuclear puncta and drives coalescence into large shell-like structures. We hypothesize that yeast lack the ideal RNA binding partners for MATR3, allowing full-length protein to form these spherical condensates, and upon complete ablation of RNA binding via RRM deletion, these condensates coalesce into a single larger structure. Further, we note that the formation of shell-like spherical condensates is not unique to TDP-43, and MATR3 also undergoes LLPS into large multiphasic shell-like condensates in the absence of RNA binding.

Potentiated Hsp104 variants suppress Matrin-3 toxicity and foci formation

Hsp104 is a potent amyloid disaggregase that solubilizes functional prions in yeast (Glover and Lindquist, 1998; Parsell et al., 1994; Shorter, 2008). Hsp104 has been shown to have limited activity in solubilizing amyloid and amyloid-like substrates associated with human disease, including TDP-43, FUS, and α -synuclein (DeSantis et al., 2012; Jackrel et al., 2014; Jackrel and Shorter, 2014a, 2014b, 2015; Lo Bianco et al., 2008). However, we have demonstrated that Hsp104 can be re-engineered to yield potentiated variants that display robust remodeling activity against a range of substrates including TDP-43, FUS, α -synuclein and TAF15 (Castellano et al., 2015; DeSantis et al., 2012; Jackrel et al., 2014; Jackrel and Shorter, 2014a, 2014b, 2015, 2017; Michalska et al., 2019; Ryan et al., 2019, 2021; Sweeny et al., 2015; Tariq et al., 2018, 2019; Yasuda et al., 2017). We therefore hypothesized that these same potentiated Hsp104 variants may also be capable of remodeling MATR3. We coexpressed MATR3^{WT} with Hsp104 and a series of potentiated variants: Hsp104^{A503V}, Hsp104^{A503S}, Hsp104^{A503G}, Hsp104^{V426L}, Hsp104^{A437W}, Hsp104^{N539K}, and Hsp104^{DPLF–A503V} which includes a range of variants that have been identified to suppress the toxicity, misfolding, and mislocalization of α -synuclein, TDP-43, and FUS (Jackrel et al., 2014; Jackrel and Shorter, 2015) (Figure 6A). Hsp104 does not suppress the toxicity of α -synuclein, TDP-43, or FUS in yeast (Jackrel et al., 2014), and we similarly find that Hsp104 does not suppress the toxicity of MATR3^{WT} (Figure 6A). In contrast, each of the potentiated Hsp104 variants tested robustly suppresses MATR3^{WT} toxicity. We observed a range in activity, with Hsp104^{A503S} and Hsp104^{V426L} displaying the most robust suppression of toxicity. To confirm that these changes are not simply due to altered expression levels, we assessed expression of MATR3^{WT} and each of the Hsp104 variants, and we observe consistent expression levels for each strain (Figure 6B). We observe decreased MATR3^{WT} levels when MATR3^{WT} is coexpressed with a potentiated variant. However, we also observe decreased expression of the Hsp104 variants themselves, suggesting that the variants are active even when expressed at lower levels than Hsp104^{WT}. These findings are consistent with previous studies with TDP-43 and FUS, where expression of potentiated Hsp104 variants decreased TDP-43 and FUS expression levels, though the stoichiometry of TDP-43 or FUS to Hsp104 variant was maintained (Jackrel et al., 2014; Jackrel and Shorter, 2014a).

We next analyzed the effects of the Hsp104 variants on formation of MATR3^{WT} foci and localization using fluorescence microscopy. Here, we analyzed two of the strongest suppressors: Hsp104^{A503S} and Hsp104^{V426L}, as well as one of the better characterized variants: Hsp104^{A503V}. We find that MATR3^{WT} forms nuclear foci that are not heavily modified by expression of Hsp104 (Figures 6C and 6D). However, upon

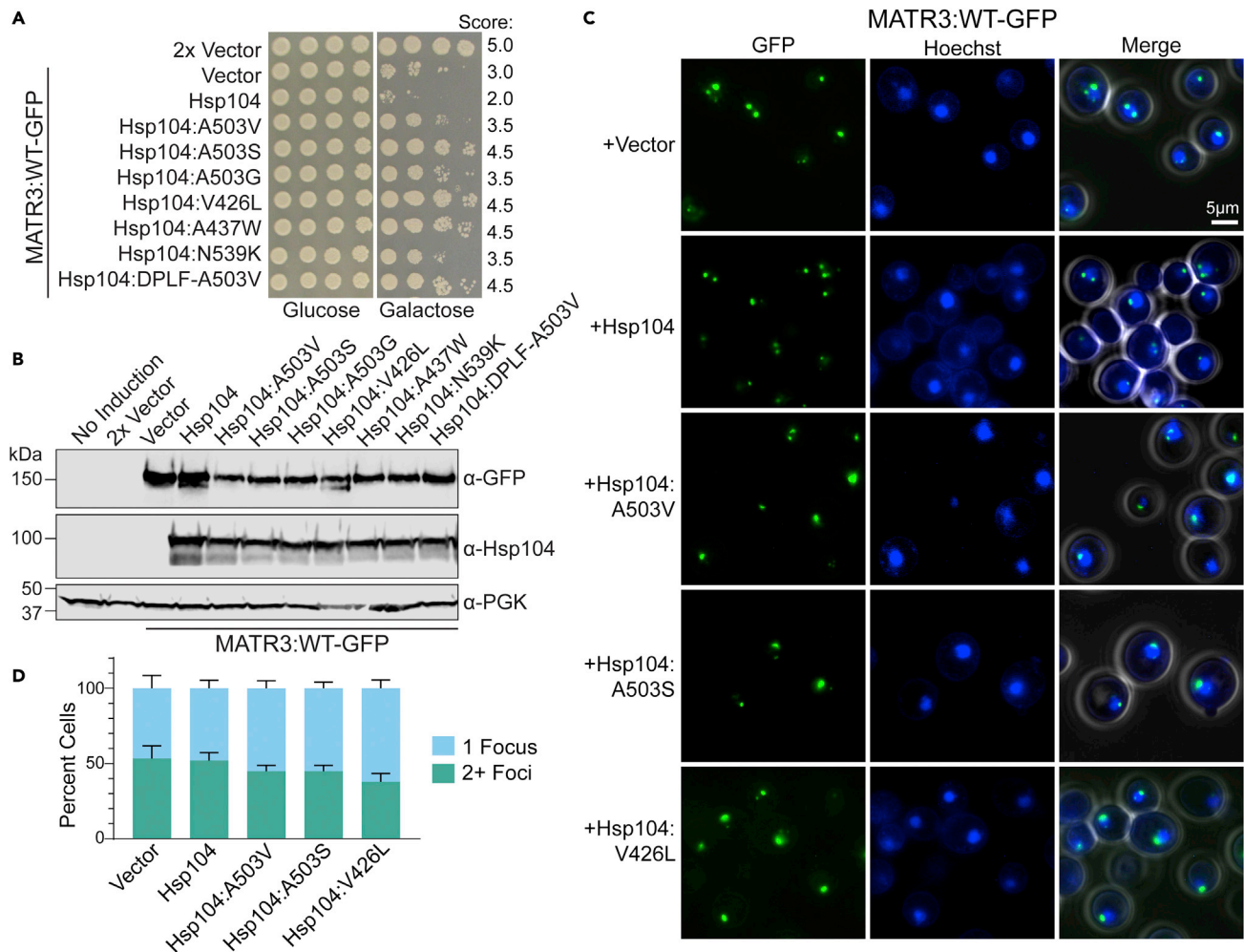


Figure 6. Potentiated Hsp104 variants suppress MATR3 toxicity and inclusion formation

(A) W303Δ*hsp104* pAG303GAL-MATR3-GFP yeast were transformed with vector, pAG416GAL-Hsp104, or the indicated variants. The strains were serially diluted 5-fold and spotted on glucose (non-inducing) or galactose (inducing) media. Scores are based on number of spots from an average of at least three replicates.

(B) Strains from A were induced for 5h, lysed, and immunoblotted for MATR3 (GFP, rabbit), Hsp104, and PGK (loading control).

(C) Select strains from A were induced for 5h, stained with Hoechst dye, and imaged. Representative images are shown. Merge channel includes GFP, Hoechst, and bright field images. Scale bar, 5µm.

(D) Quantification of the percentage of cells with one focus (light blue) or multiple foci (teal) of MATR3-GFP from microscopy experiments shown in C. N ≥ 3, with approximately 100 cells quantified per trial. Error bars show mean ± SEM.

expression of Hsp104^{A503V}, Hsp104^{A503S}, or Hsp104^{V426L} we observed an increase in the number of cells with just a single nuclear focus per cell (Figure 6C). We quantified these effects by counting the number of cells with one or more than one focus and found that there was a consistent increase in the number of cells with a single nuclear focus for each of the potentiated variants, although this trend was subtle (Figure 6D). We therefore conclude that potentiated Hsp104 variants are capable of suppressing MATR3^{WT} toxicity and foci formation.

Potentiated Hsp104 variants suppress the toxicity of MATR3 disease-associated variants

Finally, we tested if the potentiated Hsp104 variants could also suppress the toxicity of the MATR3 pathogenic variants. Here, we tested the same panel of Hsp104 variants against MATR3^{WT}, MATR3^{S85C}, MATR3^{F115C}, MATR3^{P154S}, and MATR3^{T622A} (Figure 6). Just as Hsp104 does not suppress the toxicity of MATR3, it also does not suppress the toxicity of the MATR3 variants (Figure 7A). However, the potentiated Hsp104 variants robustly suppress toxicity of each of the MATR3 variants tested. Hsp104^{A503S}, Hsp104^{V426L},

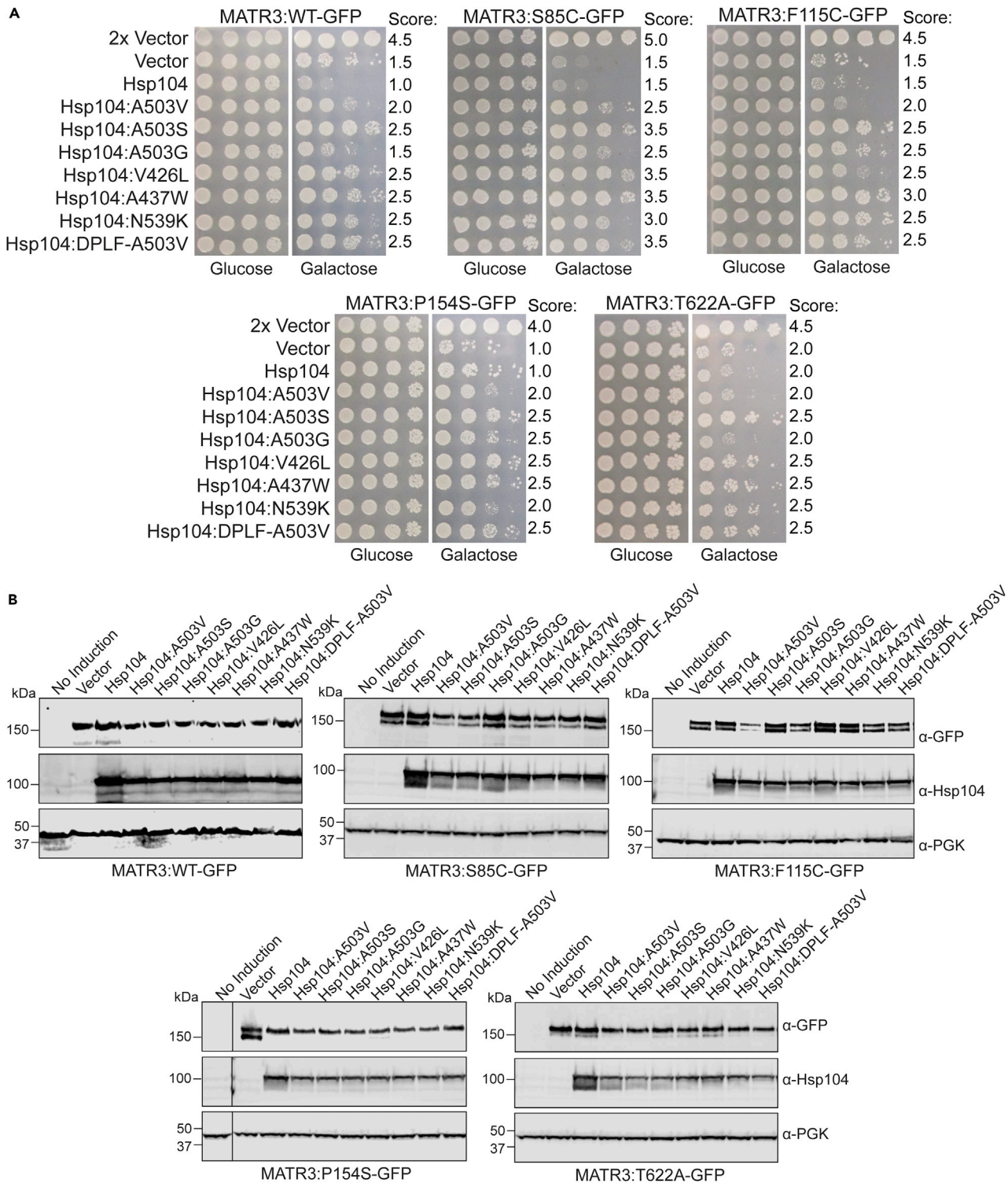


Figure 7. Potentiated Hsp104 variants suppress the toxicity of MATR3 pathogenic mutants

(A) W303Δ*hsp104* yeast were sequentially transformed with pAG423GAL-MATR3-GFP and vector, pAG416GAL-Hsp104, or the indicated variants. The strains were serially diluted 5-fold and spotted on glucose (non-inducing) or galactose (inducing) media. Scores are based on number of spots from an average of at least three replicates.

(B) Strains from A were induced for 5h, lysed, and immunoblotted for MATR3 (GFP, mouse), Hsp104, and PGK (loading control). Certain immunoblots were cropped to remove additional lanes for presentation purposes, and crop lines are marked with lines.

Hsp104^{A437W}, and Hsp104^{DPLF--A503V} displayed the strongest rescue across all MATR3 variants. Hsp104^{A503V}, Hsp104^{A503G}, and Hsp104^{N539K} conferred slightly weaker rescues across all MATR3 variants. We confirmed that expression levels of MATR3 and Hsp104 were fairly similar across the strains (Figure 7B). We therefore conclude that just as potentiated Hsp104 variants can rescue both WT and disease-linked variants of TDP-43 and FUS (Jackrel et al., 2014; Jackrel and Shorter, 2014a), they can also suppress the toxicity of both WT and disease-associated variants of MATR3.

DISCUSSION

Here, we have established a yeast model system to investigate MATR3 proteinopathy which is implicated in myopathy, ALS, and FTD (Johnson et al., 2014; Leblond et al., 2016; Lin et al., 2015; Marangi et al., 2017; Narain et al., 2019; Origone et al., 2015). We found that overexpression of human MATR3^{WT} in yeast, which lack a homolog of MATR3, confers toxicity. Similarly, overexpression of MATR3^{WT} in *Drosophila*, primary neurons, and mouse models also resulted in toxicity, shortened lifespan, and/or motor defects (Malik et al., 2018; Moloney et al., 2018; Ramesh et al., 2020; Zhang et al., 2019; Zhao et al., 2020). Staining for MATR3^{WT} in patient samples and in primary neurons shows a nuclear granular pattern (Gallego-Iradi et al., 2015, 2019; Iradi et al., 2018; Malik et al., 2018). We observe a somewhat similar nuclear staining pattern in yeast, although in yeast, MATR3^{WT} forms distinct round nuclear puncta. Overexpression of MATR3^{S85C}, MATR3^{F115C}, MATR3^{P154S}, and MATR3^{T622A}, which are linked to ALS, all displayed similar toxicity, solubility, and localization to the wild-type protein. We therefore conclude that these pathogenic mutations do not overtly destabilize MATR3. However, we do note key differences in the physical properties of the puncta comprised of the mutants and MATR3^{WT}. Overexpression of MATR3 in yeast closely recapitulates salient features reported in more complex model systems (Malik et al., 2018; Moloney et al., 2018; Ramesh et al., 2020), supporting the idea that this yeast model system can be leveraged as a useful platform for studying MATR3 misfolding in a more tractable manner.

While MATR3 is a largely disordered RBP, it is not predicted to have a prion-like domain such as those found in other disordered RBPs that underpin ALS/FTD including TDP-43 and FUS (King et al., 2012). While yeast require the disaggregase Hsp104 to regulate prions, we found that MATR3 toxicity in yeast is independent of Hsp104, similar to TDP-43 and FUS (Jackrel et al., 2014; Johnson et al., 2008). Furthermore, we find that MATR3 does not form high MW species by SDD-AGE, similar to TDP-43. It remains unclear whether the lack of a prion-like domain can drive differences in aggregation and phase separation as compared to proteins with prion-like domains, such as TDP-43 and FUS.

While we observe many similarities between MATR3^{WT} and the ALS/FTD-associated MATR3 mutants, we find that a key distinction between these proteins is their capacity to undergo liquid-liquid phase separation. We observe the formation of dynamic nuclear shell-like condensates upon expression of MATR3^{WT}, MATR3^{F115C}, and RNA-binding deficient MATR3. MATR3^{WT} yeast contains several of these structures within a single nucleus. Upon deletion of either RRM, these structures coalesce into a single larger condensate, suggesting that binding of RNA to MATR3 impairs MATR3 phase separation. We hypothesize that because yeast do not normally express MATR3, they do not have analogous RNA binding partners to those found in primary neurons, thereby allowing formation of these phase-separated condensates in yeast. To our knowledge, this is the first system in which MATR3 phase separation can be investigated with the full-length construct. Furthermore, we find that MATR3^{S85C}, MATR3^{P154S}, and MATR3^{T622A} each form gel- or solid-like puncta that are distorted and less dynamic as compared to the liquid-like spherical shell structures comprised of MATR3^{WT} and MATR3^{F115C}. Formation of these misshapen droplets confirms that the S85C, P154S, and T622A mutations each perturb the LLPS of MATR3, converting MATR3 from a liquid state to a gel- or solid-like state. Our findings are supported by previous work showing that MATR3^{S85C} can impair condensate formation and dynamics (Malik et al., 2018; Mensch et al., 2018). Importantly, in our yeast system we can distinguish the properties of the wild-type protein as compared to the pathogenic mutants S85C, P154S, and T622A while F115C does not display similar defects. In some systems no differences are noted between these four mutants, although it was recently reported that in a mouse knock-in model, the F115C mutation did not elicit a disease phenotype (van Bruggen et al., 2021). Impairment of phase separation is emerging as a key feature of ALS/FTD pathology, and now appears to also be crucial in governing MATR3 pathology (Sprunger and Jackrel, 2021). It remains to be determined when MATR3 undergoes physiological LLPS, and which specific condensates MATR3 occupies.

Strikingly, deletion of either or both RBMs leads to the formation of a single large shell-like spherical structure in the nucleus of each cell. These structures resemble the recently discovered anisosome condensates

which form upon ablation of RNA-binding in TDP-43 (Yu et al., 2021). Because these multiphasic condensates are conserved among multiple RBPs, and have been linked to chaperone proteins (Yu et al., 2021), these structures may be a crucial aspect in the mechanism mediating recovery from cellular stress. Formation of these structures suggests that MATR3 plays a role in scaffolding the condensates rather than being recruited as a client. Our results also suggest that both RRM1 and RRM2 are crucially important in MATR3 function, and that deletion of either RRM has similar effects. These results are in contrast to prior studies which suggested that RRM2 plays a more important role (Gallego-Iradi et al., 2019; Malik et al., 2018; Ramesh et al., 2020). Further investigation will be necessary to identify which physiological condensates MATR3 participates in, as well as the role of MATR3 within those condensates. It will also be important to identify the species within the MATR3 shell-like condensates, which may include Hsp70 which was identified in the core of TDP-43 anisosomes. Further, it will be important to better understand the role of these multiphasic condensates, and if these are a common structural element involved in LLPS beyond their role in MATR3 and TDP-43 (Schmidt and Rohatgi, 2016; Wang et al., 2020; Yu et al., 2021). The mechanism by which MATR3 RRMs mediate LLPS and toxicity remains unclear. It is plausible that sequestration of MATR3 to condensates buffers MATR3 toxicity or prevents aggregation of MATR3, thereby preventing MATR3 from sequestering other essential proteins.

To better understand the molecular determinants of MATR3 toxicity and foci formation as well as the contributions of its largely uncharacterized disordered regions, we generated a series of truncations and domain deletions of MATR3. We demonstrate that the minimal requirements for MATR3 toxicity are maintenance of the RRMs and NLS. We determined that MATR3 proteotoxicity is primarily driven by its RRMs, as toxicity is no longer observed upon deletion of either or both RRMs. In future work, it will be important to confirm that this toxicity is directly driven by binding of RNA to the RRMs. Alternatively, the folded RRM domains may provide crucial stabilization to an otherwise disordered protein, or mediate protein-protein interactions that drive MATR3 toxicity. We find that formation of multiple MATR3 foci is largely driven by the N-terminal disordered region, as constructs lacking this region form few or no foci. Together with our toxicity data, we conclude that MATR3 can be toxic in both the nucleus and the cytoplasm, though toxicity is greater when MATR3 is restricted to the nucleus. Further, aggregation alone is insufficient to drive toxicity.

We have also demonstrated that potentiated Hsp104 variants can suppress the toxicity of MATR3 and MATR3 mutants. These findings strongly support the idea that MATR3 toxicity is driven by corruption of proteostasis and protein misfolding, whether that be of MATR3 itself, or mediated by MATR3. We also demonstrate that potentiated Hsp104 variants decrease the number of MATR3^{WT} nuclear foci per cell. Importantly, the same Hsp104 variants which suppressed MATR3 toxicity have also been shown to suppress the toxicity, misfolding, and mislocalization of TDP-43 and FUS (Jackrel et al., 2014). Because multiple RBPs are known to aggregate in ALS/FTD, and they may behave synergistically, the solubilization of multiple RBPs by a single agent could have great therapeutic value. In this way, a single remodeling factor could be introduced to simultaneously reverse any toxic gain of function of misfolded MATR3, TDP-43, or FUS as well as any loss function due to misfolding of these RBPs.

Yeast models have been shown to be useful as highly tractable systems that can be leveraged to glean new insights into molecular determinants that drive aggregation and toxicity of proteins that misfold in disease (Elden et al., 2010; Johnson et al., 2008; Ju et al., 2011; Khurana and Lindquist, 2010; Sun et al., 2011). We have demonstrated that MATR3 proteinopathy implicated in myopathy, ALS, and FTD can be recapitulated in a novel yeast model system. Using our system, we have delineated key features driving MATR3 toxicity, aggregation, and LLPS. We anticipate that our system can be employed as a platform for rapid high-throughput screens to identify genetic or small molecule modifiers of MATR3 toxicity and aberrant LLPS. Our work has identified several potentiated Hsp104 variants which effectively suppress MATR3 toxicity, and these same variants can also reverse the proteotoxic misfolding of related proteins that drive ALS/FTD. In the future, it will be interesting to assess if these Hsp104 variants can antagonize proteotoxic misfolding in neuronal models of MATR3 proteinopathy.

Limitations of the study

Studies using a yeast model system cannot fully recapitulate all features of complex human disorders including ALS/FTD. Yet, they have been shown to be valuable systems for studying the features and malfunctioning of key genes that drive disease pathology (Couthouis et al., 2011, 2012; Elden et al., 2010; Johnson et al., 2008; Ju

et al., 2011; Kayatekin et al., 2018; Outeiro and Lindquist, 2003; Ryan et al., 2019; Sun et al., 2011; Tardiff et al., 2013; Treusch et al., 2011). Because yeast grow rapidly and are highly genetically tractable, larger numbers of constructs can be screened in yeast than is feasible in more complex model systems. It is also important to note that yeast do not naturally express MATR3. As a result, certain key RNA and protein binding partners may be absent, which could be the reason for the formation of shell-like condensates that form upon expression of MATR3^{WT} and MATR3^{F115C}. However, this limitation can also be viewed as a benefit of this system, because impaired RNA binding is thought to underpin ALS/FTD. Further, this allows for the liquid-liquid phase separation of MATR3 to be studied in a system using the full-length protein. In more complex model systems, LLPS studies of MATR3 have been restricted to use of constructs lacking the RRM, resulting in deletion of nearly all of the folded regions of MATR3 (Malik et al., 2018). As a result, we suggest that it is important that a diverse range of model systems be employed to study MATR3.

STAR★METHODS

Detailed methods are provided in the online version of this paper and include the following:

- KEY RESOURCES TABLE
- RESOURCE AVAILABILITY
 - Lead contact
 - Materials availability
 - Data and code availability
- EXPERIMENTAL MODEL AND SUBJECT DETAILS
 - Yeast strains and media
- METHOD DETAILS
 - Plasmids
 - Yeast transformation and spotting assays
 - Immunoblotting
 - Fluorescence microscopy
 - Circularity ratio
 - Fluorescence recovery after photo bleaching
 - SDD-AGE and filter retention assay
- QUANTIFICATION AND STATISTICAL ANALYSIS

SUPPLEMENTAL INFORMATION

Supplemental information can be found online at <https://doi.org/10.1016/j.isci.2022.103900>.

ACKNOWLEDGMENTS

This work was supported by NIH grant F31NS120512 (to M.L.S.), a WUSTL uSTAR Award (to K.L.), and a Target ALS Springboard Award, a Frick Foundation for ALS Research Award, ALS Association grants 20-IIA-529 and 18-IIA-408, and NIH grant R35GM128772 (to M.E.J.). We thank members of the Jackrel Lab for review of the manuscript. Confocal data were generated on a Zeiss LSM 880 Airyscan confocal microscope, which was purchased with support from the Office of Research Infrastructure Programs (ORIP), a part of the National Institutes of Health Office of the Director, under Grant OD021629.

AUTHOR CONTRIBUTIONS

Conceptualization and methodology, M.L.S. and M.E.J.; Investigation, validation, and resources, M.L.S., K.L., B.S.S., and M.E.J.; Writing, M.L.S. and M.E.J.; Supervision and project administration, M.E.J.; Funding Acquisition, M.L.S., K.L., and M.E.J.

DECLARATION OF INTERESTS

The authors declare no competing interests.

Received: October 14, 2021

Revised: January 4, 2022

Accepted: February 4, 2022

Published: March 18, 2022

REFERENCES

- Alberti, S., Gitler, A.D., and Lindquist, S. (2007). A suite of gateway cloning vectors for high-throughput genetic analysis in *Saccharomyces cerevisiae*. *Yeast* 24, 913–919.
- Alberti, S., Halfmann, R., and Lindquist, S. (2010). Biochemical, cell biological, and genetic assays to analyze amyloid and prion aggregation in yeast. *Methods Enzymol.* 470, 709–734.
- Becker, L.A., Huang, B., Bieri, G., Ma, R., Knowles, D.A., Jafar-Nejad, P., Messing, J., Kim, H.J., Soriano, A., Auburger, G., et al. (2017). Therapeutic reduction of ataxin-2 extends lifespan and reduces pathology in TDP-43 mice. *Nature* 544, 367–371.
- Belgrader, P., Dey, R., and Berezney, R. (1991). Molecular cloning of matrin 3. A 125-kilodalton protein of the nuclear matrix contains an extensive acidic domain. *J. Biol. Chem.* 266, 9893–9899.
- Boehringer, A., Garcia-Mansfield, K., Singh, G., Bakkar, N., Pirrotte, P., and Bowser, R. (2017). ALS associated mutations in matrin 3 alter protein-protein interactions and impede mRNA nuclear export. *Sci. Rep.* 7, 14529.
- Castellano, L.M., Bart, S.M., Holmes, V.M., Weissman, D., and Shorter, J. (2015). Repurposing Hsp104 to antagonize seminal amyloid and counter HIV infection. *Chem. Biol.* 22, 1074–1086.
- Coelho, M.B., Attig, J., Bellora, N., Konig, J., Hallegger, M., Kayikci, M., Eyra, E., Ule, J., and Smith, C.W. (2015). Nuclear matrix protein Matrin3 regulates alternative splicing and forms overlapping regulatory networks with PTB. *EMBO J.* 34, 653–668.
- Couthous, J., Hart, M.P., Erion, R., King, O.D., Diaz, Z., Nakaya, T., Ibrahim, F., Kim, H.-J., Mojsilovic-Petrovic, J., Panossian, S., et al. (2012). Evaluating the role of the FUS/TLS-related gene EWSR1 in amyotrophic lateral sclerosis. *Hum. Mol. Genet.* 21, 2899–2911.
- Couthous, J., Hart, M.P., Shorter, J., DeJesus-Hernandez, M., Erion, R., Oristano, R., Liu, A.X., Ramos, D., Jethava, N., Hosangadi, D., et al. (2011). A yeast functional screen predicts new candidate ALS disease genes. *Proc. Natl. Acad. Sci. U S A* 108, 20881–20890.
- Depreux, F.F., Puckelwartz, M.J., Augustynowicz, A., Wolfgeher, D., Labno, C.M., Pierre-Louis, D., Cicka, D., Kron, S.J., Holaska, J., and McNally, E.M. (2015). Disruption of the lamin A and matrin-3 interaction by myopathic LMNA mutations. *Hum. Mol. Genet.* 24, 4284–4295.
- DeSantis, M.E., Leung, E.H., Sweeny, E.A., Jackrel, M.E., Cushman-Nick, M., Neuhaus-Follini, A., Vashist, S., Sochor, M.A., Knight, M.N., and Shorter, J. (2012). Operational plasticity enables hsp104 to disaggregate diverse amyloid and nonamyloid clients. *Cell* 151, 778–793.
- Duenwald, M.L., Jagadish, S., Giorgini, F., Muchowski, P.J., and Lindquist, S. (2006). A network of protein interactions determines polyglutamine toxicity. *Proc. Natl. Acad. Sci. U S A* 103, 11051–11056.
- Elden, A.C., Kim, H.J., Hart, M.P., Chen-Plotkin, A.S., Johnson, B.S., Fang, X., Armakola, M., Geser, F., Greene, R., Lu, M.M., et al. (2010). Ataxin-2 intermediate-length polyglutamine expansions are associated with increased risk for ALS. *Nature* 466, 1069–1075.
- Feit, H., Silbergleit, A., Schneider, L.B., Gutierrez, J.A., Fitoussi, R.P., Réyes, C., Rouleau, G.A., Brais, B., Jackson, C.E., Beckmann, J.S., et al. (1998). Vocal cord and pharyngeal weakness with autosomal dominant distal myopathy: clinical description and gene localization to 5q31. *Am. J. Hum. Genet.* 63, 1732–1742.
- Franzmann, T.M., and Alberti, S. (2019). Prion-like low-complexity sequences: key regulators of protein solubility and phase behavior. *J. Biol. Chem.* 294, 7128–7136.
- Gallego-Iradi, M.C., Clare, A.M., Brown, H.H., Janus, C., Lewis, J., and Borchelt, D.R. (2015). Subcellular localization of matrin 3 containing mutations associated with ALS and distal myopathy. *PLoS ONE* 10, e0142144.
- Gallego-Iradi, M.C., Strunk, H., Crown, A.M., Davila, R., Brown, H., Rodriguez-Lebron, E., and Borchelt, D.R. (2019). N-terminal sequences in matrin 3 mediate phase separation into droplet-like structures that recruit TDP43 variants lacking RNA binding elements. *Lab. Invest.* 99, 1030–1040.
- Gietz, R.D., and Schiestl, R.H. (2007). High-efficiency yeast transformation using the LiAc/SS carrier DNA/PEG method. *Nat. Protoc.* 2, 31–34.
- Glover, J.R., and Lindquist, S. (1998). Hsp104, Hsp70, and Hsp40: a novel chaperone system that rescues previously aggregated proteins. *Cell* 94, 73–82.
- Halfmann, R., and Lindquist, S. (2008). Screening for amyloid aggregation by semi-denaturing detergent-agarose gel electrophoresis. *J. Vis. Exp.* 17, e838.
- Hayes, L.R., Duan, L., Bowen, K., Kalab, P., and Rothstein, J.D. (2020). *C9orf72* arginine-rich dipeptide repeat proteins disrupt karyopherin-mediated nuclear import. *Elife* 9, e51685.
- Hibino, Y., Ohzeki, H., Sugano, N., and Hiraga, K. (2000). Transcription modulation by a rat nuclear scaffold protein, P130, and a rat highly repetitive DNA component or various types of animal and plant matrix or scaffold attachment regions. *Biochem. Biophys. Res. Commun.* 279, 282–287.
- Iradi, M.C.G., Triplett, J.C., Thomas, J.D., Davila, R., Crown, A.M., Brown, H., Lewis, J., Swanson, M.S., Xu, G., Rodriguez-Lebron, E., et al. (2018). Characterization of gene regulation and protein interaction networks for Matrin 3 encoding mutations linked to amyotrophic lateral sclerosis and myopathy. *Sci. Rep.* 8, 4049.
- Jackrel, M.E., DeSantis, M.E., Martinez, B.A., Castellano, L.M., Stewart, R.M., Caldwell, K.A., Caldwell, G.A., and Shorter, J. (2014). Potentiated Hsp104 variants antagonize diverse proteotoxic misfolding events. *Cell* 156, 170–182.
- Jackrel, M.E., and Shorter, J. (2014a). Potentiated Hsp104 variants suppress toxicity of diverse neurodegenerative disease-linked proteins. *Dis. Model Mech.* 7, 1175–1184.
- Jackrel, M.E., and Shorter, J. (2014b). Reversing deleterious protein aggregation with re-engineered protein disaggregases. *Cell Cycle* 13, 1379–1383.
- Jackrel, M.E., and Shorter, J. (2015). Engineering enhanced protein disaggregases for neurodegenerative disease. *Prion* 9, 90–109.
- Jackrel, M.E., and Shorter, J. (2017). Protein-remodeling factors as potential therapeutics for neurodegenerative disease. *Front Neurosci.* 11, 99.
- Johnson, B.S., McCaffery, J.M., Lindquist, S., and Gitler, A.D. (2008). A yeast TDP-43 proteinopathy model: exploring the molecular determinants of TDP-43 aggregation and cellular toxicity. *Proc. Natl. Acad. Sci. U S A* 105, 6439–6444.
- Johnson, B.S., Snead, D., Lee, J.J., McCaffery, J.M., Shorter, J., and Gitler, A.D. (2009). TDP-43 is intrinsically aggregation-prone, and amyotrophic lateral sclerosis-linked mutations accelerate aggregation and increase toxicity. *J. Biol. Chem.* 284, 20329–20339.
- Johnson, J.O., Pioro, E.P., Boehringer, A., Chia, R., Feit, H., Renton, A.E., Pliner, H.A., Abramzon, Y., Marangi, G., Winborn, B.J., et al. (2014). Mutations in the Matrin 3 gene cause familial amyotrophic lateral sclerosis. *Nat. Neurosci.* 17, 664–666.
- Ju, S., Tardiff, D.F., Han, H., Divya, K., Zhong, Q., Maquat, L.E., Bosco, D.A., Hayward, L.J., Brown, R.H., Jr., Lindquist, S., et al. (2011). A yeast model of FUS/TLS-Dependent cytotoxicity. *PLoS Biol.* 9, e1001052.
- Kao, C.S., van Bruggen, R., Kim, J.R., Chen, X.X.L., Chan, C., Lee, J., Cho, W.I., Zhao, M., Arndt, C., Maksimovic, K., et al. (2020). Selective neuronal degeneration in MATR3 S85C knock-in mouse model of early-stage ALS. *Nat. Comm.* 11, 5304.
- Kayatekin, C., Amasino, A., Gaglia, G., Flannick, J., Bonner, J.M., Fanning, S., Narayan, P., Barrasa, M.I., Pincus, D., Landgraf, D., et al. (2018). Translocon declogger Ste24 protects against IAPP oligomer-induced proteotoxicity. *Cell* 173, 62–73.e69.
- Khurana, V., and Lindquist, S. (2010). Modelling neurodegeneration in *Saccharomyces cerevisiae*: why cook with baker's yeast? *Nat. Rev. Neurosci.* 11, 436–449.
- Kim, H.J., Kim, N.C., Wang, Y.D., Scarborough, E.A., Moore, J., Diaz, Z., MacLea, K.S., Freibaum, B., Li, S., Molliex, A., et al. (2013). Mutations in prion-like domains in hnRNPA2B1 and hnRNPA1 cause multisystem proteinopathy and ALS. *Nature* 495, 467–473.
- King, O.D., Gitler, A.D., and Shorter, J. (2012). The tip of the iceberg: RNA-binding proteins with prion-like domains in neurodegenerative disease. *Brain Res.* 1462, 61–80.
- Krobitsch, S., and Lindquist, S. (2000). Aggregation of huntingtin in yeast varies with the length of the polyglutamine expansion and the

- expression of chaperone proteins. *Proc. Natl. Acad. Sci. U S A* 97, 1589–1594.
- Kwiatkowski, T.J., Jr., Bosco, D.A., Leclerc, A.L., Tamrazian, E., Vanderburg, C.R., Russ, C., Davis, A., Gilchrist, J., Kasarskis, E.J., Munsat, T., et al. (2009). Mutations in the FUS/TLS gene on chromosome 16 cause familial amyotrophic lateral sclerosis. *Science* 323, 1205–1208.
- Lancaster, A.K., Nutter-Upham, A., Lindquist, S., and King, O.D. (2014). PLAAC: a web and command-line application to identify proteins with prion-like amino acid composition. *Bioinformatics* 30, 2501–2502.
- Leblond, C.S., Gan-Or, Z., Spiegelman, D., Laurent, S.B., Szuto, A., Hodgkinson, A., Dionne-Laporte, A., Provencher, P., de Carvalho, M., Orrù, S., et al. (2016). Replication study of MATR3 in familial and sporadic amyotrophic lateral sclerosis. *Neurobiol. Aging* 37, 209.e217–209.e221.
- Leonard, D., Ajuh, P., Lamond, A.I., and Legerski, R.J. (2003). hLodestar/HuF2 interacts with CDC5L and is involved in pre-mRNA splicing. *Biochem. Biophys. Res. Commun.* 308, 793–801.
- Lin, K.-P., Tsai, P.-C., Liao, Y.-C., Chen, W.-T., Tsai, C.-P., Soong, B.-W., and Lee, Y.-C. (2015). Mutational analysis of MATR3 in Taiwanese patients with amyotrophic lateral sclerosis. *Neurobiol. Aging* 36, 2005.e1–4.
- Ling, S.-C., Polymenidou, M., and Cleveland, Don W. (2013). Converging mechanisms in ALS and FTD: disrupted RNA and protein homeostasis. *Neuron* 79, 416–438.
- Lo Bianco, C., Shorter, J., Regulier, E., Lashuel, H., Iwatsubo, T., Lindquist, S., and Aebischer, P. (2008). Hsp104 antagonizes alpha-synuclein aggregation and reduces dopaminergic degeneration in a rat model of Parkinson disease. *J. Clin. Invest.* 118, 3087–3097.
- Malik, A.M., Miguez, R.A., Li, X., Ho, Y.-S., Feldman, E.L., and Barmada, S.J. (2018). Matrin 3-dependent neurotoxicity is modified by nucleic acid binding and nucleocytoplasmic localization. *Elife* 7, e35977.
- Marangi, G., Lattante, S., Doronzio, P.N., Conte, A., Tasca, G., Monforte, M., Patanella, A.K., Bisogni, G., Meleo, E., La Spada, S., et al. (2017). Matrin 3 variants are frequent in Italian ALS patients. *Neurobiol. Aging* 49, 218.e211–218.e217.
- Mensch, A., Meinhardt, B., Bley, N., Hüttelmaier, S., Schneider, I., Stoltenberg-Dinger, G., Kraya, T., Müller, T., and Zierz, S. (2018). The p.S85C-mutation in MATR3 impairs stress granule formation in Matrin-3 myopathy. *Exp. Neurol.* 306, 222–231.
- Michalska, K., Zhang, K., March, Z.M., Hatzos-Skintges, C., Pintilie, G., Bigelow, L., Castellano, L.M., Miles, L.J., Jackrel, M.E., Chuang, E., et al. (2019). Structure of *Calcarisporiella thermophila* Hsp104 disaggregase that antagonizes diverse proteotoxic misfolding events. *Structure* 27, 449–463.e447.
- Moloney, C., Rayaprolu, S., Howard, J., Fromholt, S., Brown, H., Collins, M., Cabrera, M., Duffy, C., Sieminski, Z., Miller, D., et al. (2018). Analysis of spinal and muscle pathology in transgenic mice overexpressing wild-type and ALS-linked mutant MATR3. *Acta Neuropathol. Commun.* 6, 137.
- Narain, P., Padhi, A.K., Dave, U., Mishra, D., Bhatia, R., Vivekanandan, P., and Gomes, J. (2019). Identification and characterization of novel and rare susceptible variants in Indian amyotrophic lateral sclerosis patients. *Neurogenetics* 20, 197–208.
- Neumann, M., Bentmann, E., Dormann, D., Jawaid, A., DeJesus-Hernandez, M., Ansoorge, O., Roeber, S., Kretzschmar, H.A., Muñoz, D.G., Kusaka, H., et al. (2011). FET proteins TAF15 and EWS are selective markers that distinguish FTLD with FUS pathology from amyotrophic lateral sclerosis with FUS mutations. *Brain* 134, 2595–2609.
- Neumann, M., Sampathu, D.M., Kwong, L.K., Truax, A.C., Micsenyi, M.C., Chou, T.T., Bruce, J., Schuck, T., Grossman, M., Clark, C.M., et al. (2006). Ubiquitinated TDP-43 in frontotemporal lobar degeneration and amyotrophic lateral sclerosis. *Science* 314, 130–133.
- Origone, P., Verdiani, S., Bandettini Di Poggio, M., Zuccarino, R., Vignolo, M., Caponnetto, C., and Mandich, P. (2015). A novel Arg147Trp MATR3 missense mutation in a slowly progressive ALS Italian patient. *Amyotroph. Lateral Scler. Frontotemporal Degener.* 16, 530–531.
- Outeiro, T.F., and Lindquist, S. (2003). Yeast cells provide insight into alpha-synuclein biology and pathobiology. *Science* 302, 1772–1775.
- Parsell, D.A., Kowal, A.S., Singer, M.A., and Lindquist, S. (1994). Protein disaggregation mediated by heat-shock protein Hsp104. *Nature* 372, 475–478.
- Patino, M.M., Liu, J.J., Glover, J.R., and Lindquist, S. (1996). Support for the prion hypothesis for inheritance of a phenotypic trait in yeast. *Science* 273, 622–626.
- Prilusky, J., Felder, C.E., Zeev-Ben-Mordehai, T., Rydberg, E.H., Man, O., Beckmann, J.S., Silman, I., and Sussman, J.L. (2005). FoldIndex: a simple tool to predict whether a given protein sequence is intrinsically unfolded. *Bioinformatics* 21, 3435–3438.
- Quintero-Rivera, F., Xi, Q.J., Keppler-Noreuil, K.M., Lee, J.H., Higgins, A.W., Anchan, R.M., Roberts, A.E., Seong, I.S., Fan, X., Lage, K., et al. (2015). MATR3 disruption in human and mouse associated with bicuspid aortic valve, aortic coarctation and patent ductus arteriosus. *Hum. Mol. Genet.* 24, 2375–2389.
- Ramesh, N., Kour, S., Anderson, E.N., Rajasundaram, D., and Pandey, U.B. (2020). RNA-recognition motif in Matrin-3 mediates neurodegeneration through interaction with hnRNPM. *Acta Neuropathol. Commun.* 8, 138.
- Robberecht, W., and Philips, T. (2013). The changing scene of amyotrophic lateral sclerosis. *Nat. Rev. Neurosci.* 14, 248–264.
- Ryan, J.J., Bao, A., Bell, B., Ling, C., and Jackrel, M.E. (2021). Drivers of Hsp104 potentiation revealed by scanning mutagenesis of the middle domain. *Protein Sci.* 30, 1667–1685.
- Ryan, J.J., Sprunger, M.L., Holthaus, K., Shorter, J., and Jackrel, M.E. (2019). Engineered protein disaggregases mitigate toxicity of aberrant prion-like fusion proteins underlying sarcoma. *J. Biol. Chem.* 294, 11286–11296.
- Salton, M., Elkon, R., Borodina, T., Davydov, A., Yaspo, M.-L., Halperin, E., and Shiloh, Y. (2011). Matrin 3 binds and stabilizes mRNA. *PLoS ONE* 6, e23882.
- Salton, M., Lerenthal, Y., Wang, S.-Y., Chen, D.J., and Shiloh, Y. (2010). Involvement of Matrin 3 and SFPO/NONO in the DNA damage response. *Cell Cycle* 9, 1568–1576.
- Sanchez, Y., and Lindquist, S.L. (1990). HSP104 required for induced thermotolerance. *Science* 248, 1112–1115.
- Satpute-Krishnan, P., Langseth, S.X., and Serio, T.R. (2007). Hsp104-dependent remodeling of prion complexes mediates protein-only inheritance. *PLoS Biol.* 5, e24.
- Schirmer, E.C., Homann, O.R., Kowal, A.S., and Lindquist, S. (2004). Dominant gain-of-function mutations in Hsp104p reveal crucial roles for the middle region. *Mol. Biol. Cell* 15, 2061–2072.
- Schmidt, H.B., and Rohatgi, R. (2016). In vivo formation of vacuolated multi-phase compartments lacking membranes. *Cell Rep.* 16, 1228–1236.
- Schneider, C.A., Rasband, W.S., and Eliceiri, K.W. (2012). NIH Image to ImageJ: 25 years of image analysis. *Nat. Methods* 7, 671–675.
- Senderek, J., Garvey, S.M., Krieger, M., Guergueltcheva, V., Urtizberea, A., Roos, A., Elbracht, M., Stendel, C., Tournev, I., Mihailova, V., et al. (2009). Autosomal-dominant distal myopathy associated with a recurrent missense mutation in the gene encoding the nuclear matrix protein, matrin 3. *Am. J. Hum. Genet.* 84, 511–518.
- Shorter, J. (2008). Hsp104: a weapon to combat diverse neurodegenerative disorders. *Neurosignals* 16, 63–74.
- Sprunger, M.L., and Jackrel, M.E. (2021). Prion-like proteins in phase separation and their link to disease. *Biomolecules* 11, 1014.
- Sun, Z., Diaz, Z., Fang, X., Hart, M.P., Chesi, A., Shorter, J., and Gitler, A.D. (2011). Molecular determinants and genetic modifiers of aggregation and toxicity for the ALS disease protein FUS/TLS. *PLoS Biol.* 9, e1000614.
- Sweeny, E.A., Jackrel, M.E., Go, M.S., Sochor, M.A., Razzo, B.M., DeSantis, M.E., Gupta, K., and Shorter, J. (2015). The hsp104 N-terminal domain enables disaggregase plasticity and potentiation. *Mol. Cell* 57, 836–849.
- Tada, M., Doi, H., Koyano, S., Kubota, S., Fukai, R., Hashiguchi, S., Hayashi, N., Kawamoto, Y., Kunii, M., Tanaka, K., et al. (2018). Matrin 3 is a component of neuronal cytoplasmic inclusions of motor neurons in sporadic amyotrophic lateral sclerosis. *Am. J. Pathol.* 188, 507–514.
- Tardiff, D.F., Jui, N.T., Khurana, V., Tambe, M.A., Thompson, M.L., Chung, C.Y., Kamadurai, H.B., Kim, H.T., Lancaster, A.K., Caldwell, K.A., et al. (2013). Yeast reveal a “druggable” Rsp5/Nedd4 network that ameliorates alpha-synuclein toxicity in neurons. *Science* 342, 979–983.

Tariq, A., Lin, J., Jackrel, M.E., Hesketh, C.D., Carman, P.J., Mack, K.L., Weitzman, R., Gambogi, C., Hernandez Murillo, O.A., Sweeny, E.A., et al. (2019). Mining disaggregase sequence space to safely counter TDP-43, FUS, and alpha-synuclein proteotoxicity. *Cell Rep.* 28, 2080–2095.

Tariq, A., Lin, J., Noll, M.M., Torrente, M.P., Mack, K.L., Murillo, O.H., Jackrel, M.E., and Shorter, J. (2018). Potentiating Hsp104 activity via phosphomimetic mutations in the middle domain. *FEMS Yeast Res.* 18, foy042.

Taylor, J.P., Brown, R.H., Jr., and Cleveland, D.W. (2016). Decoding ALS: from genes to mechanism. *Nature* 539, 197–206.

Treusch, S., Hamamichi, S., Goodman, J.L., Matlack, K.E.S., Chung, C.Y., Baru, V., Shulman, J.M., Parrado, A., Bevis, B.J., Valastyan, J.S., et al. (2011). Functional links between A β toxicity, endocytic trafficking, and Alzheimer's disease risk factors in yeast. *Science* 334, 1241–1245.

Tsai, W.-H. (1985). Moment-preserving thresholding: a new approach. *Computer Vis. Graphics Image Process.* 29, 377–393.

van Bruggen, R., Maksimovic, K., You, J., Tran, D.D., Lee, H.J., Khan, M., Kao, C.S., Kim, J.R., Cho, W., Chen, X.X.L., et al. (2021). MATR3 F115C knock-in mice do not exhibit motor defects or neuropathological features of ALS. *Biochem. Biophys. Res. Commun.* 568, 48–54.

Vance, C., Rogelj, B., Hortobágyi, T., De Vos, K.J., Nishimura, A.L., Sreedharan, J., Hu, X., Smith, B., Ruddy, D., Wright, P., et al. (2009). Mutations in FUS, an RNA processing protein, cause familial amyotrophic lateral sclerosis type 6. *Science* 323, 1208–1211.

Wang, C., Duan, Y., Duan, G., Wang, Q., Zhang, K., Deng, X., Qian, B., Gu, J., Ma, Z., Zhang, S., et al. (2020). Stress induces dynamic, cytotoxicity-antagonizing TDP-43 nuclear bodies via paraspeckle LncRNA NEAT1-mediated liquid-liquid phase separation. *Mol. Cell* 79, 443–458.e447.

Xu, G., Stevens, S.M., Jr., Kobeissy, F., Brown, H., McClung, S., Gold, M.S., and Borchelt, D.R. (2012). Identification of proteins sensitive to thermal stress in human neuroblastoma and glioma cell lines. *PLoS ONE* 7, e49021.

Xu, L., Li, J., Tang, L., Zhang, N., and Fan, D. (2016). MATR3 mutation analysis in a Chinese cohort with sporadic amyotrophic lateral sclerosis. *Neurobiol. Aging* 38, 218.e213–218.e214.

Yasuda, K., Clatterbuck-Soper, S.F., Jackrel, M.E., Shorter, J., and Mili, S. (2017). FUS inclusions disrupt RNA localization by sequestering kinesin-1 and inhibiting microtubule dytrosination. *J. Cell Biol.* 216, 1015–1034.

Yokom, A.L., Gates, S.N., Jackrel, M.E., Mack, K.L., Su, M., Shorter, J., and Southworth, D.R. (2016). Spiral architecture of the Hsp104 disaggregase reveals the basis for polypeptide translocation. *Nat. Struct. Mol. Biol.* 23, 830–837.

Yu, H., Lu, S., Gasior, K., Singh, D., Vazquez-Sanchez, S., Tapia, O., Toprani, D., Beccari, M.S., Yates, J.R., Da Cruz, S., et al. (2021). HSP70 chaperones RNA-free TDP-43 into anisotropic intranuclear liquid spherical shells. *Science* 371, eabb4309.

Zeitz, M.J., Malyavantham, K.S., Seifert, B., and Berezney, R. (2009). Matrin 3: chromosomal distribution and protein interactions. *J. Cell Biochem.* 108, 125–133.

Zhang, X., Yamashita, S., Hara, K., Doki, T., Tawara, N., Ikeda, T., Misumi, Y., Zhang, Z., Matsuo, Y., Nagai, M., et al. (2019). A mutant MATR3 mouse model to explain multisystem proteinopathy. *J. Pathol.* 249, 182–192.

Zhao, M., Kao, C.S., Arndt, C., Tran, D.D., Cho, W.I., Maksimovic, K., Chen, X.X.L., Khan, M., Zhu, H., Qiao, J., et al. (2020). Knockdown of genes involved in axonal transport enhances the toxicity of human neuromuscular disease-linked MATR3 mutations in *Drosophila*. *FEBS Lett.* 594, 2800–2818.

STAR★METHODS

KEY RESOURCES TABLE

REAGENT or RESOURCE	SOURCE	IDENTIFIER
Antibodies		
Rabbit polyclonal anti-Hsp104	Enzo	ADI-SPA-1040
Mouse monoclonal anti-PGK	Invitrogen	459250
Rabbit monoclonal anti-MATR3 N-terminus	Abcam	Ab151739
Rabbit polyclonal anti-GFP	Sigma	G1544
Mouse monoclonal anti-GFP	Roche	1184-460-001
Goat anti-rabbit secondary antibody	Li-cor	926-68071
Goat anti-mouse secondary antibody	Li-cor	926-32210
Bacterial and virus strains		
XL10-Gold cells	Agilent	230245
One Shot TOP10 Chemically competent <i>E. coli</i>	Invitrogen	C404010
Chemicals, peptides, and recombinant proteins		
PfuUltra II Fusion HS DNA Polymerase	Agilent	600672
DpnI	New England Biolabs	R0176S
BP clonase	Invitrogen	11789020
LR clonase	Invitrogen	11791020
Experimental models: Organisms/strains		
<i>S. cerevisiae</i> : W303a (<i>MATa</i> , <i>can1-100</i> , <i>his3-11, 15</i> , <i>leu2-3, 112</i> , <i>trp1-1</i> , <i>ura3-1</i> , <i>ade2-1</i>)	Schirmer et al. (2004)	N/A
<i>S. cerevisiae</i> : W303aΔ <i>hsp104</i> (<i>MATa</i> , <i>can1-100</i> , <i>his3-11, 15</i> , <i>leu2-3, 112</i> , <i>trp1-1</i> , <i>ura3-1</i> , <i>ade2-1</i> , <i>hsp104::KanMX</i>)	Schirmer et al. (2004)	N/A
<i>S. cerevisiae</i> : W303aΔ <i>hsp104</i> -pAG303GAL-TDP-43-YFP	Aaron Gitler	N/A
<i>S. cerevisiae</i> : W303a-pAG303GAL-FLAG-103Q-GFP	James Shorter	N/A
Recombinant DNA		
MATR3 cDNA	Dharmacon	MHS6278-202757255
pDONR221-ccdB	Invitrogen	12536017
pAG416GAL-ccdB	Alberti et al. (2007)	N/A
pAG413GAL-ccdB	Alberti et al. (2007)	N/A
pAG423GAL-ccdB-EGFP	Alberti et al. (2007)	N/A
pAG303GAL-ccdB-EGFP	Alberti et al. (2007)	N/A
pDONR-221-MATR3 WT	This paper	N/A
pDONR-221-MATR3:S85C	This paper	N/A
pDONR-221-MATR3:F115C	This paper	N/A
pDONR-221-MATR3:P154S	This paper	N/A
pDONR-221-MATR3:T622A	This paper	N/A
pDONR-221-MATR3 WT (no stop codon)	This paper	N/A
pDONR-221-MATR3:S85C (no stop codon)	This paper	N/A
pDONR-221-MATR3:F115C (no stop codon)	This paper	N/A
pDONR-221-MATR3:P154S (no stop codon)	This paper	N/A

(Continued on next page)

Continued

REAGENT or RESOURCE	SOURCE	IDENTIFIER
pDONR-221-MATR3:T622A (no stop codon)	This paper	N/A
pAG413GAL-MATR3 WT	This paper	N/A
pAG413GAL-MATR3:S85C	This paper	N/A
pAG413GAL-MATR3:F115C	This paper	N/A
pAG413GAL-MATR3:P154S	This paper	N/A
pAG413GAL-MATR3:T622A	This paper	N/A
pAG423GAL-MATR3-eGFP	This paper	N/A
pAG423GAL-MATR3:S85C-eGFP	This paper	N/A
pAG423GAL-MATR3:F115C-eGFP	This paper	N/A
pAG423GAL-MATR3:P154S-eGFP	This paper	N/A
pAG423GAL-MATR3:T622A-eGFP	This paper	N/A
pDONR-221-MATR3(1-397)	This paper	N/A
pDONR-221-MATR3(1-575)	This paper	N/A
pDONR-221-MATR3(398-595)	This paper	N/A
pDONR-221-MATR3(398-847)	This paper	N/A
pDONR-221-MATR3(576-847)	This paper	N/A
pAG423GAL-MATR3(1-397)-eGFP	This paper	N/A
pAG423GAL-MATR3(1-575)-eGFP	This paper	N/A
pAG423GAL-MATR3(398-595)-eGFP	This paper	N/A
pAG423GAL-MATR3(398-847)-eGFP	This paper	N/A
pAG423GAL-MATR3(576-847)-eGFP	This paper	N/A
pAG423GAL-MATR3 Δ 398-473-eGFP	This paper	N/A
pAG423GAL-MATR3 Δ 496-575-eGFP	This paper	N/A
pAG423GAL-MATR3 Δ 588-595-eGFP	This paper	N/A
pAG423GAL-MATR3 Δ 398-473, Δ 496-575-eGFP	This paper	N/A
pAG416GAL-Hsp104	Jackrel et al. (2014)	N/A
pAG416GAL-Hsp104:A503V	Jackrel et al. (2014)	N/A
pAG416GAL-Hsp104:A503S	Jackrel et al. (2014)	N/A
pAG416GAL-Hsp104:A503G	Jackrel et al. (2014)	N/A
pAG416GAL-Hsp104:V426L	Jackrel et al. (2014)	N/A
pAG416GAL-Hsp104:A437W	Jackrel et al. (2014)	N/A
pAG416GAL-Hsp104:N539K	Jackrel et al. (2014)	N/A
pAG416GAL-Hsp104:Y257F-A503V-Y662F	Jackrel et al. (2014)	N/A
Software and algorithms		
Image J	Schneider et al. (2012)	https://imagej.nih.gov/ij/
GraphPad Prism	GraphPad	Version 9.0

RESOURCE AVAILABILITY

Lead contact

Further information and requests for resources and reagents should be directed to and will be fulfilled by the lead contact, Meredith Jackrel (mjackrel@wustl.edu).

Materials availability

Plasmids newly generated in this study will be made readily available to the scientific community. Material transfers will be made with no more restrictive terms than in a Materials Transfer Agreement.

Data and code availability

All data reported in this paper will be shared by the lead contact upon request.

This paper does not report original code.

Any additional information required to reanalyze the data reported in this paper is available from the lead contact upon request.

EXPERIMENTAL MODEL AND SUBJECT DETAILS

Yeast strains and media

All yeast were WT W303a (*MATa*; *can1-100*; *his3-11,15*; *leu2-3,112*; *trp1-1*; *ura3-1*; *ade2-1*) or the isogenic strain W303 Δ *hsp104* (Sanchez and Lindquist, 1990). Yeast were grown in rich medium (yeast extract, peptone, dextrose (YPD)) or in synthetic media lacking the appropriate amino acids. Media was supplemented with 2% glucose, raffinose, or galactose. W303 Δ *hsp104*-pAG303GAL-TDP-43-YFP and W303WT-pAG303GAL-FLAG-103Q-GFP were provided by Dr. Aaron Gitler and Dr. James Shorter, respectively.

METHOD DETAILS

Plasmids

Human MATR3 cDNA was obtained from Dharmacon (MHS6278-202757255) and inserted into pDONR221-ccdB via Gateway BP reaction. The entry clone was used to transfer MATR3 to suitable yeast expression vectors (pAG413GAL-ccdB, pAG423GAL-ccdB-EGFP, pAG303GAL-ccdB-EGFP). MATR3 mutations were generated using Quikchange site-directed mutagenesis (Agilent). Separate entry clones were generated by PCR to produce MATR3(1-397), MATR3(1-575), MATR3(398-595), MATR3(398-847), and MATR3(576-847) in pDONR-221-ccdB. These truncations were then transferred to 423GAL-ccdB-eGFP by LR reaction. Deletion constructs MATR3^{ANLS} (amino acid residues 588-595), MATR3^{ARRM1} (amino acid residues 398-473 deleted), MATR3^{ARRM2} (amino acid residues 496-575 deleted), and MATR3^{ARRM1/2} (amino acid residues 398-473 and 496-575 deleted) were generated using Quikchange site-directed mutagenesis (Agilent). All MATR3 constructs were confirmed by DNA sequencing. pAG416GAL-Hsp104 and potentiated variants were generated previously (Jackrel et al., 2014).

Yeast transformation and spotting assays

Yeast were transformed according to standard protocols using polyethylene glycol and lithium acetate (Gietz and Schiestl, 2007). In brief, the indicated yeast strains were grown to early log phase, harvested, and washed with sterile water. The yeast were then resuspended in a 360 μ L transformation mixture containing 33% polyethylene glycol 3350, 0.1M lithium acetate, and 0.1 mg boiled single-stranded salmon sperm DNA. The indicated MATR3 expression vectors were then added and mixtures were incubated at 42°C for 20 min. Yeast were then harvested, washed, and plated on appropriate dropout media. For strains harboring both MATR3 and Hsp104, MATR3 was transformed first, transformants were harvested from selective media, and strains were subsequently transformed with pAG416GAL-Hsp104 plasmids. W303 Δ *hsp104*-pAG303GAL-MATR3-GFP was generated by linearizing pAG303GAL-MATR3-GFP with NheI followed by transformation into W303 Δ *hsp104*. For spotting assays, yeast were grown to saturation overnight in raffinose-supplemented dropout media at 30°C. Cultures were normalized to $A_{600nm} = 1.50$, serially diluted 5-fold, and spotted in duplicate onto synthetic dropout media containing glucose or galactose. Plates were analyzed after 2-3 days of growth at 30°C. Each experiment was repeated with at least three independent transformations. Yeast growth on galactose plates were scored on a scale of 0-6 using half integers from no growth to full growth. The averages from all trials were rounded to the nearest half integer for reporting.

Immunoblotting

Yeast were grown overnight in raffinose supplemented media and then induced with galactose for 5h at 30°C. Cultures were normalized to $A_{600nm} = 0.5$, 9 mL cells were harvested, treated in 0.1M NaOH for 5min at room temperature, and cell pellets were then resuspended into 1x SDS sample buffer and boiled for 3min. Lysates were cleared by centrifugation, separated by SDS-PAGE (4–20% gradient, BioRad), and transferred to a PVDF membrane. Membranes were blocked in Odyssey Blocking Buffer (LI-COR) for 1h at room temperature. Primary antibody incubations were performed at 4°C overnight. Membranes were

incubated in secondary antibodies for 1h at room temperature. Membranes were imaged using a LI-COR Odyssey FC Imaging system. Antibodies used: rabbit anti-MATR3_{N-terminus} monoclonal (Abcam), rabbit anti-GFP polyclonal (Sigma Aldrich), mouse anti-GFP monoclonal (Roche Applied Science), rabbit anti-Hsp104 polyclonal (Enzo Life Sciences), mouse anti-PGK monoclonal (Invitrogen), and fluorescently labeled anti-mouse and anti-rabbit secondary antibodies (LI-COR).

Fluorescence microscopy

For fluorescence microscopy, the indicated strains were grown and induced as described above for immunoblotting. After a 5 h induction at 30°C, cultures were harvested, and live cells were treated with Hoechst dye to visualize the nuclei. Images were collected at 100x magnification using a Nikon Eclipse Te2000-E microscope, a Nikon A1 Confocal LSM, or a Zeiss LSM 880 Airyscan confocal microscope and processed using ImageJ software. All experiments were repeated at least three times, and representative images are shown. For quantification, at least one hundred cells were manually counted per strain per trial to quantify number of foci or localization of MATR3-GFP.

Circularity ratio

The circularity ratio is a measurement of how round an object appears, taken as the ratio of the object's area to the area of a perfect circle with the same perimeter as the given object. A perfectly circular object has a ratio of one, while less circular objects trend towards a ratio of zero. The circularity ratio is calculated by:

$$\text{Circularity ratio} = 4\pi \left(\frac{\text{Area}}{\text{Perimeter}^2} \right)$$

Circularity ratios of foci were measured from deconvolved confocal slices by auto-thresholding in ImageJ using the Moments method (Tsai, 1985). The area and perimeter of each focus was measured, which was then used to calculate circularity ratio.

Fluorescence recovery after photo bleaching

For FRAP experiments, the indicated strains were grown and induced as described above for immunoblotting. After a 5 h induction at 30°C, cultures were harvested, and live cells were immobilized between a 4% low-temperature agarose pad and coverslip, which was then sealed with nail polish. Cells were imaged on a Zeiss LSM 880 Confocal Microscope with Airyscan operated by Zen Black using an alpha Plan-Apochromat 100x oil objective. A horizontal 1 × 25 pixel line was drawn across the center of the foci. After acquisition of five pre-bleach images, ROIs were photobleached using a 488nm laser at 70% power and a 405nm laser at 1% power for 50 iterations of 16 μsec per pixel. Fluorescence recovery was monitored for 2min at 1.29 sec/frame after bleaching using the Airyscan detector. Images were deconvolved with a 6.9 Airyscan parameter.

Image analysis was conducted in FIJI. While the cells were immobilized in the agarose pad, movement of the foci within the cells precluded the data from quantitative analysis. A trial required that the recovery of the focus or lack thereof remained within the field of view for the duration of analysis. At least ten trials were acquired for each strain. Representative images are shown for one trial of each strain.

SDD-AGE and filter retention assay

The indicated strains were grown and induced as described above for immunoblotting. After a 5 h induction at 30°C, 5mL of cells at A_{600nm} = 0.5 were harvested and washed with sterile water. The cell pellet volume was approximated and resuspended in a 5x volume of native lysis buffer (50mM HEPES, pH 7.5, 150mM NaCl, 2.5mM EDTA, 1% triton-X-100, 10mM BME, 0.1mM PMSF, 5uM pepstatin A, 1% yeast protease inhibitor cocktail (Sigma)) and one volume of acid-washed glass beads. Lysis was completed by alternating 30s of vortexing with 30s recovery on ice for ten minutes. Cell debris was pelleted at 2000 xg for 5 min and supernatant was diluted with 2x sample buffer (80mM Tris-HCl, pH 6.8, 10% glycerol, 0.2% bromophenol blue) supplemented with 0-4% SDS as indicated for 1x final concentration.

For semi-denaturing detergent agarose gel electrophoresis (SDD-AGE) (Alberti et al., 2010; Halfmann and Lindquist, 2008), samples were resolved on a horizontal 1% agarose gel in 20mM Tris, 200mM glycine, and 0.1% SDS at 4°C. The gels were then transferred onto a PVDF membrane in a modified Mini Trans-Blot cell at 4°C. Proteins were detected by immunoblotting as described above.

For filter retention assays (Alberti et al., 2010), cellulose acetate (CA) membranes were washed in PBST and then placed on top of filter paper in a Minifold I 96-well spot-blot array system (GE). 30 μ L of each prepared lysate was applied to the CA membrane in triplicate, drawn through the system, and then wells were washed with PBST. For nitrocellulose (NC) binding, samples were spotted in triplicate onto NC membranes. Membranes were allowed to dry, washed in PBST, blocked, and imaged by immunoblotting as described above. Bound protein was quantified using ImageStudio Lite software (LI-COR). For quantifying the amount of aggregated protein, the GFP signal of the CA membrane was divided by the GFP signal of the NC membrane and normalized to TDP-43-YFP. Four biological replicates were completed with three technical replicates per blot. Comparisons were made using a one-way ANOVA with a Dunnett's multiple comparisons test.

QUANTIFICATION AND STATISTICAL ANALYSIS

As described in the figure legends, all data points in each graph are means \pm standard error of the mean (SEM). For yeast experiments, n represents a biological replicate. For microscopy experiments, n represents a single cell. N is indicated in the figure legends. Statistical analysis was performed using a one-way ANOVA with a Dunnett's multiple comparisons test. p-values are shown in the figure legends, with $p > 0.05$ designated as non-significant.